Alleviating Tropical Atlantic Sector Biases in the Kiel Climate Model by Enhancing Horizontal and Vertical Atmosphere Model Resolution: Climatology and Interannual Variability

Jan Harlaß[1], Mojib Latif[1,2], and Wonsun Park[1]

[1]GEOMAR Helmholtz Centre for Ocean Research Kiel, Kiel, Germany

[2]Kiel University, Kiel, Germany

Corresponding author address: Jan Harlaß, GEOMAR, Duesternbrooker Weg 20, 24105 Kiel, Germany.

E-mail: jharlass@geomar.de

Abstract

We investigate the quality of simulating tropical Atlantic (TA) sector climatology and interannual variability in integrations of the Kiel Climate Model (KCM) with varying atmosphere model resolution. The ocean model resolution is kept fixed. A reasonable simulation of TA sector annual-mean climate, seasonal cycle and interannual variability can only be achieved at sufficiently high horizontal and vertical atmospheric resolution. Two major reasons for the improvements are identified. First, the western equatorial Atlantic westerly surface wind bias in spring can be largely eliminated, which is explained by a better representation of meridional and especially vertical zonal momentum transport. The enhanced atmospheric circulation along the equator in turn greatly improves the thermal structure of the upper equatorial Atlantic with much reduced warm sea surface temperature (SST) biases. Second, the coastline in the southeastern TA and steep orography are better resolved at high resolution, which improves wind structure and in turn reduces warm SST biases in the Benguela upwelling region.

The strongly diminished wind and SST biases at high atmosphere model resolution allow for a more realistic latitudinal position of the Intertropical Convergence Zone. Resulting stronger cross-equatorial winds, in conjunction with a shallower thermocline, enable a rapid cold tongue development in the eastern TA in boreal spring. This enables simulation of realistic interannual SST variability and its seasonal phase locking in the KCM, which primarily is the result of a stronger thermocline feedback. Our findings suggest that enhanced atmospheric resolution, both vertical and horizontal, could be a key to achieving more realistic simulation of TA climatology and interannual variability in climate models.

Keywords

Tropical Atlantic SST bias Benguela

Climate Modelling Resolution GCM biases

1. Introduction

Simulating tropical Atlantic (TA) sector climate and its variability is a long-standing problem in coupled atmosphere-ocean general circulation models (CGCMs, Davey et al. 2002). Persistent biases degrade seasonal forecasts (e.g. Repelli & Nobre 2004; Stockdale et al. 2006) and undermine the credibility of climate change projections (e.g. Ashfaq et al. 2011; Wan et al. 2011) for a region where a large rural population critically depends on rain for agriculture. For example, large warm biases amounting to several centigrade are found in the sea surface temperature (SST) of the two upwelling systems in the eastern TA. One upwelling system is in the eastern equatorial Atlantic (EEA), referred to as the equatorial cold tongue. The SSTs in the cold tongue region depict a pronounced seasonal cycle with the cold tongue developing in boreal spring and lasting through summer. This also is the time of strong interannual SST variability in that region. SSTs in the EEA influence amongst others the West African Monsoon system (e.g. Brandt et al. 2011; Caniaux et al., 2011) and thus Sahel rainfall (Giannini et al. 2003). The other upwelling system is in the Benguela Current region off the coast of southwestern Africa, and this region too is a major problem area with much too warm SSTs in CGCMs.

The SST annual cycle in the TA originates from large-scale atmosphere-ocean-land- interactions. TA SSTs reach a maximum in boreal spring, when the Intertropical Convergence Zone (ITCZ) is close to and surface winds are weak at the equator. As the ITCZ moves northward during the course of the year and the West African Monsoon sets in, southeasterly winds in the EEA cross the equator and strengthen. This drives upwelling (downwelling) slightly south (north) of the equator, increased vertical mixing in the ocean, and enhanced evaporation subsequently cooling the equatorial ocean (Philander and Pacanowski, 1981). Such wind induced changes are strongest in the EEA, since the thermocline is shallowest there. The resulting zonal SST gradient induces an atmospheric pressure gradient that strengthens the easterly trade winds at the equator, thereby helping to transport the cooling signal to the west (Mitchell and Wallace, 1992; Xie, 1994). Meridional transport of zonal momentum in the lower atmosphere and zonal pressure gradient related to monsoon rainfall distribution join in to accelerate easterly winds and further support the westward propagating signal (Okumura and Xie, 2004).

The two regions, EEA and South Eastern Topical Atlantic (SETA), are not independent of each other. Strength and position of the South Atlantic Cyclone impacts both timing of the cold tongue onset in the EEA (Caniaux et al., 2011) and SST anomalies in the SETA (Lübbecke et al., 2010). The oceanic pathway consists of eastward propagating equatorial Kelvin waves (EKW) excited by equatorial zonal wind stress anomalies that displace the thermocline vertically (Servain et al., 1982; Hormann and Brandt, 2009) and travel southward along the African coast as coastally trapped Kelvin waves (CTW, Bachèlery et al., 2015; Richter et al., 2011; Toniazzo & Woolnough, 2013; Voldoire et al., 2014; Wahl et al., 2011; Xu et al., 2014).

State-of-the-art climate models struggle to realistically represent the TA mean climate and TA variability. Most models are unable to simulate the cold tongue development and often even show a reversed zonal SST gradient along the equator due to large warm biases in the EEA and SETA (e.g. Davey et al., 2002; Richter & Xie, 2008). Even though climate models underwent substantial development, the warm bias problem is seen in models participating in the Coupled Model Intercomparison Project phase 5 (CMIP5, Richter et al., 2012) in addition to an offset SST error in the tropical mean SST (Li and Xie, 2012). The flawed climatology hinders simulation of realistic interannual SST variability and its pronounced seasonal phase locking in many climate models (see Ding et al., 2015a, 2015b for the KCM), which may be one important reason for the low seasonal prediction skill in the TA attained with the these models.

Several studies link the EEA warm bias to a westerly wind bias at the equator during boreal spring (DeWitt, 2005; Chang et al., 2007; Richter and Xie, 2008; Richter et al., 2011, 2012; Tozuka et al., 2011; Wahl et al., 2011; Patricola et al., 2012; Zermeño-Diaz and Zhang, 2013). The westerly wind bias is already present in uncoupled atmosphere general circulation model (AGCM) integrations with specified observed SSTs (Chang et al. 2007; Richter and Xie 2008; Chang et al. 2008) and thought to be linked to erroneous zonal sea level pressure (SLP) gradients due to rainfall errors. Another possible cause for the westerly wind bias is an erroneous momentum flux from the free troposphere into the well mixed boundary layer (Zermeño-Diaz and Zhang 2013; Richter et al. 2014). Further, CGCMs produce excessive rainfall south of the equator, referred to as the so-called double ITCZ problem (Stockdale et al. 2006; Deser et al. 2006; Breugem et al. 2006; Richter and Xie 2008; Richter et al. 2012), that due to air-sea interactions exacerbates errors from AGCMs when run in coupled mode.

The warm SST bias in the SETA has been attributed to the structure of the alongshore surface winds driving coastal upwelling and too little low-level stratus cloud cover causing a surplus of solar insolation at the sea surface (Huang et al. 2007; Huang and Hu 2007; Xu et al. 2014a). Large and Danabasoglu (2006) and Wahl et al. (2011) show that radiation errors alone cannot completely explain the warm SST bias. Hourdin et al. (2015) underlines the importance of relative humidity and evaporation for the warm SST bias.

In this paper, we follow the approach to reduce model biases in the TA by systematically increasing the resolution, both horizontal and vertical, of the atmospheric component of the Kiel Climate Model (KCM), while keeping the resolution of the ocean component fixed. Several studies have employed a similar strategy but without much success in reducing the TA warm SST bias (Patricola et al. 2012; Delworth et al. 2012; Doi et al. 2012; Small et al. 2014). Harlaß et al. (2015) show the key to succeed is keeping consistency between horizontal and vertical atmosphere model resolution and to enhance resolution in the lower troposphere. We show that improving the atmospheric circulation by enhancing the resolution of the atmospheric component of the KCM largely eliminates the SST biases in the TA and also greatly improves the simulation of interannual variability in the TA.

The paper is organized as follows: Section 2 provides a brief description of the model and the experimental setup. In Section 3, the results for the TA climatology are described, the results for the TA interannual variability in Section 4. The paper is concluded by a summary and discussion of the major results in Section 5.

2. Model and experimental setup

We use the Kiel Climate Model (KCM, Park et al. 2009), a coupled atmosphere-ocean-sea ice general circulation model. The atmosphere model component is ECHAM5 (Roeckner et al. 2003) with varying resolution, as described below. The ocean-sea ice component NEMO (Madec 2008) is integrated on a tripolar grid (ORCA2 grid) and is kept unchanged at a horizontal resolution of 2° x 2°, with a latitudinal refinement of 0.5° in the equatorial region (15°S-15°N). It has 31 sigma levels and resolves the upper 100 m with 10 m spacing. The coupling interval is once a day.

Four experiments have been performed with the coupled model, in which only the atmospheric resolution varies (Table 1). Horizontal resolution has been increased from T42 (~2.8°) to T255 (~0.47°), with either 31 (L31) or 62 (L62) vertical levels. The top level in the atmosphere remains similar: for L31 and L62 at 10 hPa and 5 hPa, respectively. There are 6 levels below 850 hPa in L31, but 14 levels in L62. The additional levels are placed between the original ones. Parametrization schemes, as for example cloud microphysics and optical properties or cumulus convection, are scale-aware in ECHAM5 (Roeckner et al. 2003) and vary with resolution but are not re-tuned.

We additionally performed atmosphere-only runs at the same resolutions to separate the influences of atmosphere model biases from those due to coupling. The uncoupled atmosphere model integrations are forced by NOAA Optimum Interpolation 1/4° daily SST and sea ice data version 2 (Reynolds et al. 2007; Reynolds 2009) covering the period 1982-2009.

Horizontal Resolution	**Grid points Lon × Lat**	**Vertical Resolution**	**Acronym Coupled**	**Acronym Uncoupled**
T042, ~2.80°	128 x 64	31	L	L (A)
T159, ~0.75°	480 x 240	31	M	M (A)
T159, ~0.75°	480 x 240	62	M-V	M-V (A)
T255, ~0.50°	768 x 384	62	H-V	-

Table 1 Model configurations of the KCM analyzed in this study.

The following reanalysis data are used in the investigations below: European Centre for Medium-Range Weather Forecasts (ECMWF) Re-Analysis for 1982-2009 on a 0.75° grid (ERA-interim, Dee et al. 2011), 40-yr European Centre for Medium-Range Weather Forecasts Re-Analysis for 1958-2001 on a 0.5° grid (ERA-40, Uppala et al. 2005), NOAA-CIRES 20th Century Reanalysis version 2 for 1982-2009 on 2° grid (20CRv2, Compo et al. 2011), Simple Ocean Data Assimilation version 2.0.2 for 1958-2001 on a 0.5° grid (SODA, Carton and Giese 2008).

Observational datasets are: the Met Office Hadley Centre EN3 version 2a for 1955-2010 on a 1° grid (HadEN3, Guinehut et al. 2009), Met Office Hadley Centre SST for 1982-2009 on a 1° grid (HadISST, Rayner 2003), NOAA Optimum Interpolated SST v2 for 1982-2009 on a 0.25° grid (NOAA-OISST, Reynolds et al. 2007; Reynolds 2009), Cross-Calibrated Multi-Platform surface winds for 1988-2014 on a 0.25° grid (CCMP2.2, Wentz et al. 2015), Scatterometer Climatology of Ocean Winds (SCOW, Risien and Chelton 2008) using QuickSCAT measurements, Clouds and the Earth's Radiant Energy System Energy Balanced And Filled surface fluxes for 2001-2015 on a 1° grid (CERES EBAF-Surface Ed2.8, Kato et al. 2013), Woods Hole Oceanographic Institution objectively analyzed air-sea fluxes for 1984-2009 on a 1° grid (OAFlux, Yu et al. 2008), Global Precipitation Climatology Project v2.2 for 1982-2009 on a 2.5° (GPCP2, Adler et al. 2003), Tropical Rainfall Measuring Mission 3B43 for 1998-2014 on a 0.25° grid (TRMM, Huffman et al. 2007).

Finally, we use the multi-model ensemble-mean of historical simulations over the period 1870-2004 conducted with 17 models participating in the Coupled Model Intercomparison Project phase 5 (CMIP5, Taylor et al. 2012), all interpolated onto a T42 grid.

To study the spatial structure of the interannual variability simulated in the different integrations we performed linear regression analysis using some key indices and monthly data. We also employ the Bjerknes (BJ) index to investigate in a compact way the feedbacks simulated in the different versions of the KCM. The BJ index is based on the recharge oscillator framework for ENSO (Jin et al. 2006) and was originally developed to study equatorial Pacific interannual variability. Lübbecke and McPhaden (2013), hereafter LMP13, were the first to apply the BJ index to the TA and we use that methodology. The BJ index includes the zonal advection feedback (ZAF), Ekman feedback (EF), thermocline feedback (TF), dynamical damping (DD) and thermal damping (TD). The formulation of the positive feedbacks (ZAF, EF and TF) is based on mean-state variables and a series of coefficients that measure the sensitivity of the atmosphere (i.e. zonal wind stress) to SST changes, and the ocean (i.e. zonal currents, upwelling and thermocline tilt) to changes in the zonal wind stress. The negative feedbacks (DD and TD) describe the damping effects on SST anomalies from mean ocean currents and changes in atmospheric heat fluxes. Table 2 gives an overview of the feedback terms contributing to the BJ index. The sum of all feedbacks defines the BJ index which thus is a measure of coupled ocean-atmosphere stability or the growth rate of SST anomalies. All data is detrended and a 3-month running mean applied prior to analysis to damp high-frequency fluctuations. Volume average is taken over the Atlantic 3 region (ATL3; 20°W-0°W, 3°S-3°N) and from the surface to the mixed layer depth (MLD), defined as the depth where the temperature deviates by not more than 0.2 K from the SST. Zonal wind stress anomalies are averaged over the equatorial Atlantic (40°W-0°W, 3°S-3°N) and thermocline depth is estimated as the depth of the 23°C-isotherm, following LMP13. Statistical significance is assessed with a two tailed t-test.

Contributing feedbacks	**Formulation**
Zonal advection feedback (ZAF)	$\mu_a \beta_u \left\langle \frac{-\partial \bar{T}}{\partial x} \right\rangle_E$
Ekman feedback (EF)	$\mu_a \beta_w \left\langle \frac{-\partial \bar{T}}{\partial z} \right\rangle_E$
Thermocline feedback (TF)	$\mu_a \beta_h \left\langle \frac{H(\bar{w})\bar{w}}{H_m} a_h \right\rangle_E$
Dynamical damping (DD)	$-\left(\frac{\langle \bar{u} \rangle_E}{L_x} + \frac{\langle -2y\bar{v} \rangle_E}{{L_y}^2} + \frac{\langle \bar{w} \rangle_E}{H_m} \right)$
Thermal damping (TD)	α

Table 2 Contributing feedbacks in the Bjerknes index and their formulation. μ_a denotes equatorial zonal wind stress response to eastern equatorial SST anomalies, β_u zonal ocean velocity response, β_w ocean upwelling response and β_h thermocline slope response to equatorial zonal wind stress anomalies. a_h is the ocean subsurface temperature response to thermocline depth anomalies and α the net surface heat flux response to SST anomalies. $\bar{u}, \bar{v}, \bar{w}$ denote mean zonal, meridional and vertical ocean velocities, $\bar{T}$ mean SST and H_m mean mixed layer depth. $\langle\cdot\rangle_E$ denotes volume-averaged quantities over the eastern equatorial regime with L_x and L_y as zonal and meridional extent. $H(\acute{w})$ is a step function to account only for upstream vertical advection. The responses are estimated via linear regressions. Methodology adapted from (Lübbecke and McPhaden 2013).

3. Climatology

Atmosphere

Boreal spring and boreal summer are the two seasons which are very difficult to simulate in climate models. In boreal spring (March-April-May MAM, Fig. 1a), SSTs in the central equatorial Atlantic (CEA) are at their maximum, the

ITCZ is at its southern most position and close to the equator, and Trade winds in the western TA converge at the equator. Zonal winds are very weak there, as are cross-equatorial winds in the EEA. It is especially the surface winds during boreal spring that precondition the ocean state along the equator and thereby determine the strength of coupled feedbacks in the following summer.

As mentioned above, many state-of-the-art climate models have large difficulties in simulating boreal spring surface climate, as demonstrated by the ensemble-mean SST biases of the CMIP5 models analyzed here (Fig. 1b, color shading). We note that the globally averaged SST has been removed from all observational and model datasets before computing biases to account for the different mean states in the models. The ensemble-mean SSTs in the coastal upwelling areas of the Northern Hemisphere (NH) and Southern Hemisphere (SH) are much too high, reaching biases of more than 7 K in the Benguela upwelling area, presumably due to too weak alongshore winds. Off-equatorial western TA SSTs are too cold with typical biases of 1 K in the northwest. The ITCZ is located too far south (Fig. 1b, contours), thereby inhibiting easterly surface winds in the EEA and in turn equatorial upwelling, which gives rise to a warm SST bias on the order of 1 K that intensifies near the coast. Additionally, a large dry bias over South America is evident.

The picture derived from the lowest resolution version of the KCM (experiment L, Fig. 1c) is rather similar to that obtained from the CMIP5 models. There are, however, noticeable differences. For example, stronger westerly winds and more rainfall over the EEA are simulated. When increasing the horizontal resolution to T159, but keeping the coarse vertical resolution (experiment M, Fig. 1d), SST biases only slightly reduce. The dry bias over northern South America reduces due to increased large-scale precipitation at orography (not shown), the wet bias over the Gulf of Guinea becomes smaller, and the excessive rainfall band moves slightly northward in the western TA. The western equatorial Atlantic (WEA) westerly wind bias remains.

SST biases are substantially reduced only when we additionally enhance the vertical resolution from L31 to L62 (experiment M-V, Fig. 1e), especially in the coastal upwelling regions of the eastern TA. Further improvement is seen at a horizontal resolution of T255 with a vertical resolution of L62 (experiment H-V, Fig. 1f), most notably in the eastern TA where also the cold NH SST bias near 20°N strongly reduces.

SSTs in the EEA and along the coast of southwestern Africa reach their minimum during boreal summer (July-August-September JAS), which is associated with the development of the cold tongue, and the ITCZ is at its most northern position (Fig. 2a). The CMIP5 models' warm SST biases are largest during boreal summer and cover the entire EEA and SETA (Fig. 2b) as it is the case in L (Fig. 2c). Increased horizontal resolution in M reduces the warm SST bias (Fig. 2d). Further reduction of the warm SST bias is achieved when additionally enhancing the vertical resolution (M-V, Fig. 2e), and the bias becomes still smaller when going to even higher horizontal resolution (H-V, Figs. 2f). The SST biases diminish to less than 2 K over most parts of the TA in H-V, which is a major advance upon L (Fig. 2c).

The much reduced warm SST bias enables a sufficiently northward position of the ITCZ which is simulated at about the correct position in H-V, although with larger rain rates than observed especially over the ocean, a known feature of the atmosphere model ECHAM5 (Biasutti et al. 2006; Hagemann et al. 2006). Once again, it is only the atmosphere model resolution that was varied in the experiments; the ocean model resolution was kept identical. A major result from this study is that enhancing atmosphere model resolution, both horizontal and vertical, seems to be a key to significantly reduce Tropical Atlantic sector surface climate biases.

The seasonal migration of the ITCZ is crucial to the development of the cold tongue. Cross-equatorial (Trade) winds, associated with an ITCZ located sufficiently north, generate coastal upwelling and thereby cool the surface (Philander and Pacanowski 1981). The ITCZ in the EEA is predominantly located in the NH, it only extends into the SH during boreal winter and spring (Figs. 3a,b). The two investigated observational datasets differ mainly in rainfall magnitude, with TRMM having a larger maximum in May/June (Fig. 3b). Cross-equatorial winds are weak during boreal spring and become much stronger in May/June. The lowest-resolution model L simulates a too southern rainfall band all year round (Fig. 3c), which is associated with a lack of cross-equatorial winds during boreal winter and spring. Instead westerly winds are simulated at the equator. The rainfall band narrows at higher horizontal resolution (M, Fig. 3d) and the two rainfall maxima are better represented. Although the SST bias in the SETA is somewhat reduced (Figs. 1d, 2d), the remaining SST bias still prevents the northward extension of rainfall into the Sahel region (Steinig et al. 2017, in prep.) and cross-equatorial winds are still poorly simulated in boreal spring. A sufficiently northern position of the ITCZ in boreal summer and only slightly overestimated rainfall south of the equator during boreal winter and spring only is simulated in M-V and H-V (Figs. 3e,f), the two model configurations which employ the higher vertical resolution L62.

Furthermore, the overall three-dimensional wind structure is well reproduced at L62, as shown for boreal spring (Fig. 4). In particular, at high vertical resolution easterly surface winds become strong enough in boreal spring and boreal summer (Fig. 5a) to generate sufficient equatorial upwelling which cools the surface. This is one reason for the steep seasonal cycle of SST in the ATL3 region being well reproduced in M-V and H-V (Fig. 5h, red and purple lines). Higher vertical resolution helps to strengthen cross-equatorial winds, whereas a higher horizontal resolution improves the space-time structure of rainfall (in terms of latitudinal position and double maximum), as can be inferred from H and H-V (Figs. 3e,f). Rainfall rates are in general too high over the Gulf of Guinea and further increase with higher horizontal resolution (Figs. 1,2). This also is the case in the corresponding AGCM-only simulations with observed SSTs (not shown). In the uncoupled AGCM experiments, however, the overall space-time structure of rainfall is well simulated even at lower resolution, but the second rainfall maximum in boreal summer only develops in M-V(A), and enhanced vertical resolution does again help to strengthen the cross-equatorial winds in late boreal spring.

Steinig et al. (2017, in prep.) in a forthcoming paper presents the sensitivity of the West African Monsoon and associated Sahel rainfall to atmosphere model resolution using the same simulations as those discussed here.

A latitude-height section in the western TA (40°W-10°W) shows the large extent of significant zonal wind (color shading) from the surface up to about 250 hPa during boreal spring (MAM) in reanalysis (Figs. 4a,b). Zonal wind is larger near the surface in the SH than in the NH. There is, however, some uncertainty. For example, 20CRv2 provides a twice as strong zonal wind at about 700 hPa (Fig. 4b). The zonal wind in the equatorial region is reversed and westerly at the surface in L (Fig. 4c), and these westerlies extend to a height of about 700 hPa in the SH. Outside the equatorial region, zonal wind is reasonably well simulated. The westerly bias is still present in M (Fig. 4d), and also M-V but with further reduced magnitude (Fig. 4e). Only experiment H-V, the simulation with high horizontal *and* vertical resolution, has an overall good representation of the zonal wind at all heights (Fig. 4f).

Meridional winds converge north of the equator at 4°N (Figs. 4a,b), and this is the location of maximum rainfall (red line in Fig. 4, right scale). As for zonal wind, there is some uncertainty in the rainfall data. The TRMM dataset is much better resolved than GPCP, but only available for a short time period, and has a larger maximum than that in GPCP. Further, TRMM depicts a secondary maximum slightly south of the equator (Fig. 4a). All KCM configurations overestimate rainfall in the SH (red dashed lines in Figs. 4c-f). In line with that, vertical velocities are too strong south of the equator. Excessive rainfall in the SH is somewhat reduced and two maxima are simulated in H-V, with one maximum in the NH (Fig. 4f), indicating some improvement relative to the model versions with coarser resolution.

In order to understand the westerly surface wind bias in the equatorial region we next investigate zonal equatorial SLP, SST and precipitation gradients between the eastern and western part of the basin. The convention is that a negative (positive) SLP gradient would induce westerly (easterly) wind. In contrast, a negative (positive) SST gradient would induce easterly (westerly) winds, as would a negative (positive) precipitation gradient. Observations indicate that zonal wind is easterly all year-round and weakest in boreal spring (black line in Fig. 5a). The easterly flow in boreal spring is against the SLP (Fig. 5c) and SST (Fig. 5g) gradients, both favoring westerly winds. Only the equatorial precipitation gradient tends to support easterlies in boreal spring (Fig. 5e).

A surface wind bias over the WEA in boreal spring also is seen in the uncoupled AGCM simulations (Fig. 5b). The SST gradient in these integrations by definition is realistic, the SLP gradient reasonably well simulated (Fig. 5d) and not sensitive to changes in resolution. However, the precipitation gradient independent of resolution depicts the wrong sign during boreal spring (Fig. 5f), which counteracts the effects of the SST and SLP gradients. It is interesting to note, that the zonal wind and the SLP gradient are in line in the rest of the year, while only in boreal spring SLP gradient is negative and zonal wind is at its minimum. Independent of resolution zonal wind is more negative (Fig. 5b), as SLP gradient is more positive (Fig. 5d), except for spring, in the uncoupled simulations, still zonal wind changes with resolution. Thus, the weakening of zonal wind in boreal spring is in line with the SLP forcing, plus an additional modification as for example advection/entrainment of zonal easterly momentum. A stronger consistency between zonal wind at 850hPa and the SLP gradient throughout our uncoupled configurations further supports this (Fig. S3a,b).

Richter et al. (2014) found no dominant impact of zonal SLP and SST gradients on easterly surface winds in MAM (nor their climatology and variability) either. They propose a large role of meridional and more importantly downward zonal momentum transport from the free troposphere to maintain the easterly surface winds. The westerly wind bias is linked in Richter et al. (2014) to excessive rainfall over the ocean south of the equator and deficient rainfall over equatorial South America. We find precipitation over these regions does hardly change with increased resolution (not shown) but the westerly bias significantly reduces, suggesting a larger influence of maximum rainfall position and vertical zonal momentum transport at higher resolution. This is further supported by the well resolved easterly jet at 700 hPa north of the equator, while there are much larger wind biases south of the equator at a similar height and below (Figs. 4c-f). Richter et al. (2014) additionally emphasize the large contribution of internal atmospheric variability to the free troposphere influence on the boundary layer, which we conjecture has to be adequately resolved. Further analysis of the processes contributing to the zonal momentum budget, such as vertical mixing, and the use of a boundary layer model (as in Stevens et al. 2002) are required to shed more light on this issue.

Vertical winds in the western TA north of the equator also strengthen with increased atmosphere model resolution in the uncoupled simulations, leading to two rainfall maxima almost symmetrically located about the equator (not shown). This goes in line with stronger southerly winds which transport zonal momentum directly into regions of largest westerly wind bias. Zermeño-Diaz and Zhang (2013) could not find such a relationship between the ITCZ and westerly wind bias in AGCMs, but they also highlight the deficient entrainment of zonal momentum from the free troposphere into the boundary layer, even in the case of well reproduced total rainfall amounts and diabatic heating profiles over equatorial South America. Vertical transport of zonal momentum is tightly connected to convective activity, which is important for the impact of zonal momentum transport, meridional and vertical, on surface winds (and the ocean) in areas with maximum rainfall. In the KCM version H-V, using the highest horizontal and vertical resolution, meridional winds, uplift and maximum rainfall in the WEA are simulated at about the correct location and with realistic strength, as are the easterlies (Fig. 4f).

During boreal spring SLP, precipitation and SST gradients (Figs. 5c,e,g) favor westerly flow in L and M, which the models seem not to be able to withstand. The SST gradient is weaker than observed but still positive in M-V and H-V in boreal spring, the two experiments in which zonal winds have the correct sign (Fig. 5a). Thus, the SST gradient cannot account for the westerly surface wind bias in boreal spring. The SLP gradients simulated during boreal spring are more negative than observed, but improve at higher resolution (Fig. 5c). Changes among the different KCM versions are most prominent for the zonal precipitation gradient that switches sign from positive in L, M and M-V, supporting westerly winds, to negative in H-V, supporting easterly winds, (Fig. 5e). In summary, although all three zonal gradients help achieving easterly surface flow in boreal spring, the precipitation gradient seems to be the most important contributor.

Surprisingly, zonal wind in boreal summer, autumn and winter is easterly in L and M (green and red lines in Figs. 5a,c,e,g), albeit an almost zero SLP gradient and positive SST and precipitation gradients, the latter two both inducing westerly flow. This underlines the role of other processes affecting the seasonal cycle of equatorial zonal wind such as the interaction of equatorial Atlantic SSTs with the West African Monsoon. Okumura and Xie (2004) conducted experiments without a seasonal cold tongue development and still zonal wind anomalies appeared in the EEA in May and June due to zonal momentum transport across the equator and redistribution of rainfall patterns.

Equatorial Atlantic

Improvements in the simulation of the Tropical Atlantic Ocean in response to enhancing atmosphere model resolution are as remarkable as those in the atmosphere. As noted above, the ocean model configuration was not changed and kept at 2°×2° resolution in all integrations of the KCM. We investigate the seasonal evolution of the depth of the 23°C-isotherm (Z-23, Fig. 6). In the TA, Z-23 can be used as a proxy for thermocline depth and upper ocean heat content. Data from SODA (Fig. 6a) and HadEN3 (Fig. 6b) indicate that the equatorial (3°N-3°S) thermocline is deep in the west and shoals towards the east throughout the calendar year. Z-23 reaches a maximum (minimum) in the west during boreal summer and fall (spring). The annual-mean slope is a result of the integrated effect of equatorial zonal wind stress and seasonal depth variations are strongly linked to zonal wind stress variations during the course of a year. A sudden onset of cross-equatorial winds in relation to the northward displacement of the ITCZ induces surface cooling via Ekman upwelling south of the equator, increases vertical mixing and also enhances evaporation over the EEA. The resulting change in SST gradient (Fig. 5g) weakens (strengthens) the easterlies in boreal spring (summer) in the central and western equatorial Atlantic thereby propagating the cooling signal to the west. Positive (negative) zonal wind stress anomalies induce downward (upward) eastward traveling EKWs that deepen (shoal) the thermocline to the east and warm (cool) the SST, especially in the east where the thermocline is shallow.

In experiments L and M (Figs. 6c,d) Z-23 is too shallow in the west, in line with too weak zonal wind stress and too deep Z-23 in the east, except in boreal winter, resulting in a too small thermocline tilt across the equator. Enhanced easterly wind stress in M-V and H-V (Figs. 6e,f) significantly lowers thermocline depth in the west while it is hardly changed in the east, thereby creating a stronger west-east tilt in Z-23. A much too deep thermocline in the east during boreal spring exists in all simulations, with H-V depicting the smallest bias. The reason likely is the reversal of the easterly wind stress in the CEA in March/April that excites downwelling EKWs which deepen the thermocline in the east approximately 1 to 2 months later. At the same time, local Ekman pumping due to too strong westerly wind stress in the very east further deepens the thermocline there. A delay time of 1 to 2 months to account for crossing the equator is consistent with observational studies (Servain et al. 1982; Keenlyside and Latif 2007). The theoretical phase speed of the second baroclinic Kelvin wave of 1.2 to 1.5 m/s, considered to be dominant in the EEA (Doi et al. 2007; Polo et al. 2008), would yield a crossing time of about 1 month.

Two further features are noted. First, maximum thermocline tilt occurs about 1-2 months later in the simulations with the KCM in comparison to SODA and HadEN3. Second, the shallowest Z-23 in SODA and HAdEN3 is close to the coast in July/August, whereas it is shifted into the ocean interior in the model runs and simulated in September/October. This could be the result of spurious waves originating in the CEA excited by zonal wind stress biases. The eastward traveling Kelvin wave signal is reflected at the African coast, partly travels back as Rossby waves and displaces the Z-23 maximum in all model integrations to about 10°W.

The SST bias in boreal spring in the lowest-resolution configuration (L, Fig. 1c) is small at the equator in the east and negative (cold bias) in the west. However, the longitude-depth section along the equator reveals the existence of a strong subsurface warm bias in the east in experiments L and M-V (Figs. 7a,c). This warming is related to the too deep thermocline, as indicated by Z-23 (Figs. 6c,e). The subsurface bias in the east is smaller in experiment M (Fig. 7b) in which the thermocline depth bias is also smaller (Fig. 6d). In experiment H-V (Fig. 7d), the subsurface temperature bias is almost absent. We note that full temperatures and thermocline depth peak in May (not shown).

The western cold bias increases with depth, reaching its maximum at 90 m depth in experiment L (Fig. 7a). Increased horizontal resolution in the atmosphere only slightly reduces the cold bias (M, Fig. 7b). Higher vertical atmosphere model resolution in M-V and H-V (Figs. 7c,d) eliminates the western cold bias by lowering the thermocline in the west (Figs. 6e,f). Although temperature biases are strongly alleviated in H-V, a cold bias is still observed near the surface and a warm bias below the mixed layer. This could be an indication of too strong vertical mixing in the ocean, which would diffuse the thermal structure, an effect that does not clearly show up if thermocline tilt is strongly biased.

In SODA, the core of the eastward flowing Equatorial Undercurrent (EUC) resides at about 35°W and 60 m depth with a peak velocity of 60 cm/s, and the EUC extends over almost the entire basin and displayed depth range (Fig. 7e). Upper ocean zonal currents are not well simulated in experiments L and M (contours, Figs. 7a,b). The zonal currents in L are unrealistically strong at the surface in the eastern basin and an undercurrent only is seen in west. Peak velocities are 20 cm/s at 35°W at about 50 m depth, but 40 cm/s at 10°E near the surface. The near-surface maximum reduces in M (Fig. 7b), but the current structure basically remains as in L. Experiments M-V and H-V (Figs. 7c,d) show large improvements in the zonal currents. EUC core velocities increase to 35 and 45 cm/s in M-V and H-V, respectively, and the eastward current extends to larger depth. Noticeable differences to SODA remain. However, biases in SODA also may contribute to these differences.

During boreal spring, the WEA experiences easterly winds, the CEA predominantly northward winds and the EEA very weak westerly winds (Figs. 6a,b). This leads in SODA to strong upwelling in the western part of the basin and weak downwelling near the African coast (vectors, Fig. 7e). The westerly surface wind bias in L and M (Figs. 6c,d) results in too weak upwelling in the west and even in downwelling in the CEA and EEA (Figs. 7a,b) due to the reversal of zonal winds (Figs. 6c,d). Only H-V depicts a reasonable representation of vertical velocities in the EEA that is somewhat consistent with SODA (Fig. 7d). Enhanced easterly wind stress owing to higher vertical atmosphere model resolution in M-V and H-V (Figs. 6e,f) strengthens upwelling (Figs. 7c,d) to a similar level as in SODA (Fig. 7e).

Benguela upwelling region

Largest SST biases in the Benguela upwelling region generally are seen during boreal summer. Three major mechanisms have been suggested to play a role in that area: i) excessive net surface shortwave radiation due to too little low-level cloud cover, ii) remote influences by advection of subsurface biases (meridional current) and wave propagation (vertical current), and iii) insufficient representation of meridional current structure. Regarding errors in marine stratocumulus clouds, all our model configurations simulate too little cloud cover (not shown). In fact the only noticeable changes in the surface heat budget originate from reduced sensible and latent heat fluxes in M-V and H-V (not shown) as a result of the much smaller SST biases (Figs. 1e,f, 2e,f). The remaining summer SST bias of 1-2 K may be due to the low-level cloud cover bias and possibly too weak offshore advection.

To explore remote influences on the Benguela upwelling region we depict meridional sections averaged over a 4° longitude band along the African coast (Fig. 8). While in experiment L the SST bias is strongest in boreal summer (Fig. 8a), there is a much stronger temperature bias below the surface in boreal spring (Fig. 8e), as in many state-of-the-art models (i.e. in CMIP5; Xu et al. 2014b; Xu et al. 2014a; Toniazzo and Woolnough 2013). We only show for boreal spring the lowest-resolution KCM configuration L, since the biases are strongest in that simulation. The mechanisms outlined below are similar in the other experiments but with smaller amplitude. As in the equatorial Atlantic, M-V and H-V feature the smallest upper ocean temperature biases (Figs. 8c,d). In theory, EKWs forced in the WEA/CEA would need about 1-2 months to reach the eastern coast where part of the energy is reflected into southward traveling CTWs. It approximately takes one month for CTWs to arrive at the northern Benguela upwelling region (Bachèlery et al. 2015), and about another month until the wave signal influence the SST (Florenchie et al. 2004). These considerations also suggest a remote contribution of equatorial wind stress biases during boreal spring to the temperature biases along the African coast in JAS in the simulations with the KCM. Fig. 8. highlights the limited southward propagation range of CTWs in our model at around 15°S, in line with previous studies (Bacherlery et al., 2015; Florenchie et al., 2004; Polo et al., 2008). The remotely forced bias remains at higher resolution as the equatorial region is still biased to some extend, while the local bias south of 15°S is largely eliminated.

The spatial structure and temporal variability of coastal currents and upwelling zones in ocean models is very sensitive to the nearshore wind pattern. We investigate wind stress, wind stress curl (WSC) and depth-integrated (15 m – 216 m) meridional velocities in boreal summer (JAS, Fig. 9), when SST biases are largest. The WSC pattern at low atmosphere model resolution (L, Fig. 9d) is far too broad compared to QuikSCAT, ERA-interim and SODA (Figs. 9a-c). The resulting strong southward coastal current at depth (Fig. 9i) as well as a southward surface current (not shown) are consistent with a Sverdrup balance-governed situation in L (Small et al. 2015). Comparing the wind stress and WSC patterns in M, M-V and H-V (Figs. 9e-g) to those in L, coastal trapping of WSC south of about 15°S is clearly visible and related to the much better resolved orography at higher horizontal resolution. This in turn weakens the Sverdrup balance-related flow there, and equatorward subsurface currents (Figs. 9j-l) as well as surface currents (not shown) develop. Larger WSC in H-V strengthens the poleward flow, while larger wind stress strengthens the Benguela current flowing equatorward in M-V and H-V. Although wind stress and WSC patterns are much more realistic, the coarse ocean model resolution of 2° inhibits the simulation of the narrow structure of the coastal currents and their strength.

The improved currents due to enhanced wind stress and WSC at higher horizontal resolution clearly impacts SST (Figs. 9o-q) and the subsurface temperature bias (Figs. 8b-d) along the African coast in M, M-V and H-V by advecting less (more) warm (cold) water from the north (south) into the Benguela upwelling system. In L the erroneous southward current (Fig. 9i) advects the subsurface warm bias signal (Fig. 8a,e), originating from the equatorial region, into the upwelling region where it contributes to the severe warm bias. A small change in the latitudinal position of the so-called Angola-Benguela-Front has a large effect on SST. The remaining SST bias to a large part is confined to the coast. Here, due to the coarse ocean model resolution, vertical velocity (Fig. 8) cannot benefit from the improved wind stress pattern at higher atmosphere model resolution. The vertical velocity increases from L to M but shows only minor changes when further enhancing the atmosphere model resolution in M-V and H-V. Small et al. (2015) showed that a realistic WSC pattern along the African coast via sufficient atmosphere model resolution needs an eddy resolving ocean to well simulate the Benguela upwelling system. A recent study by Patricola and Chang (2016) highlights the importance of atmosphere resolution to resolve the narrow band of WSC associated with the Benguela low-level jet. Krebs et al. (2017, submitted), using an ocean-only model set up with realistic wind forcing, support the need for higher horizontal ocean model resolution by showing that a 1/10° resolution is necessary to realistically simulate coastal upwelling.

4. Interannual variability

Fig. 10 presents the long-term standard deviation of monthly SST anomalies in the ATL3 region as a function of the calendar month. There is a marked seasonal phase locking in the observations (black line). SST variability starts to rise from low levels in April, reaches its maximum in June and decreases thereafter until it again reaches low levels in September. We note a small secondary variability maximum in November to January. Experiments L and M employing low vertical resolution (L31) in the atmosphere model depict weak SST variability in the ATL3 region throughout the year and thus fail to simulate seasonal phase locking. In contrast, the KCM versions with higher vertical atmosphere model resolution (L62) do feature seasonal phase locking with a summer peak of similar magnitude as observed. However, there is a delay such that the summer peak occurs 2 months (1 month) after the observed peak in experiments M-V (H-V). The delay amounts to 3 months when the KCM is integrated in an L-V (T42 L62) configuration (Harlaß et al. 2015, Fig. S3). Thus, seasonal SST phase locking in the ATL3 region only is simulated when the vertical resolution of the atmosphere model amounts to L62. Increasing the horizontal atmosphere model resolution reduces the delay of the variability maximum at high vertical atmosphere model resolution, suggesting that both high vertical and horizontal atmosphere model resolution are important to realistically simulate seasonal SST phase locking in the ATL3 region. This is further illustrated by regressing basin-wide SST anomalies on the ATL3 SST anomaly index that emphasizes the large-scale character of the interannual variability with two distinct maxima in the CEA and SETA, which is only realistically simulated in terms of pattern and amplitude at higher vertical atmosphere resolution (Fig. S1).

In observations the surface wind response to ATL3 SST anomalies, as shown by linear regression, is larger in magnitude and spatial extent in the NH than in the SH (Figs. 11a,b). In the latter, the wind response is mostly confined to the WEA and westerly anomalies dominate just south of the equator. Experiments L and M (Figs. 11c,d) show a predominantly meridional wind response north of the equator, missing the important zonal component to weaken the easterly Trades, and do not capture the SH response in the WEA. Experiments M-V and H-V show a more realistic response in terms of wind direction and area extending from the Brazilian coast to about 10°W, but partly overestimate surface wind strength (Figs. 11e,f). H-V outperforms M-V with regard to the latitudinal position of strongest zonal wind anomalies located directly south of the equator. Surface wind anomalies also differ among configurations when the atmosphere model is forced by observed SSTs (Fig. S2). Experiment L(A) shows a too strong (weak) response of the zonal (meridional) wind anomalies, M(A) only reduces these biases in the SH, and M-V(A) has the most reasonable surface wind response. This seems to have a beneficial effect in coupled mode.

The rainfall anomaly pattern associated with ATL3 SST variability reveals an increase along the equator and south of it in the western TA (Figs. 11a,b). Reduced rainfall is observed north of the main positive anomaly, indicating a southward shift of the ITCZ. The largest rainfall anomaly occurs west of the ATL3 region. All model configurations overestimate the magnitude of rainfall anomalies in coupled (Figs. 11c-f) and uncoupled (Fig. S2) mode, a common bias in atmosphere models (Biasutti et al. 2006). Experiments L and M simulate strong equatorial rainfall anomalies that extend into the ATL3 region and fail to reproduce the rainfall anomalies in the east north of the equator (Figs. 11c,d). Experiments M-V and H-V also exhibit noticeable biases depicting only weak signals over South America and a concentration of rainfall anomalies north of the equator, but they simulate a reasonable rainfall response in the EEA (Figs. 11e,f). The lack of anomalous rainfall over South America also is evident in the uncoupled AGCM runs with prescribed observed SSTs (Fig. S2). The erroneous pattern over the South American continent in M-V and H-V is linked to the locally insufficient diabatic heating in response to ATL3 SST variability (not shown).

We next investigate the 3-dimensional wind response to ATL3 SST anomalies, as illustrated by a latitude-height section at 40°W (Fig. 12). This is important to understand the surface wind anomalies. Zonal wind anomalies (color shading) obtained from ERA-interim (Fig. 12d) depict a baroclinic response with anomalous westerlies in the lower and anomalous easterlies in the upper troposphere, consistent with Xie and Carton (2004). The easterly anomalies are more confined to the equatorial region in comparison to the westerly anomalies. The uncoupled AGCM simulations (Figs. 12a-c) can represent gross aspects of the observed pattern. The coupled simulations at low vertical atmosphere model resolution L and M (Figs. 12e,f), perform very poorly, possibly also because they fail to simulate strong interannual SST variability. The L62 coupled model versions M-V and H-V (Figs. 12g,h) reproduce the observed response pattern well, but with smaller amplitude in the upper troposphere.

The zonal wind response is essentially symmetric about the equator, whereas the meridional and vertical wind response is asymmetric (Fig. 12d). Predominantly meridional winds up to about 700 hPa blowing towards the equator in the SH is observed, while there is a weak but significant downward component in the NH, increasing with height. Surface wind convergence is observed south of the equator producing uplift. Only the higher-resolution uncoupled AGCM runs (Figs. 12b,c) reproduce the meridional wind response south and north of the equator down to the surface, and only experiment M-V(A) shows the downward motion in the NH (Fig. 12c). Since experiments M(A) and M-V(A) better represent the ITCZ in the WEA (not shown), they also generate an uplift signal just south of the equator. This is missing in the coupled simulations M-V and H-V (Figs. 12g,h), because of the absent rainfall response in that area (Figs. 11e,f). Instead, the response is shifted further to the east. Meridional and vertical wind anomalies in experiments M-V and H-V are consistent with observations, with H-V being the more realistic simulation.

The above analysis suggests that two anomalous wind systems need to be resolved in the WTA. First, the near-surface wind anomalies in and slightly above the boundary layer blowing in both hemispheres from the subtropics towards the equator. Second, the anomalous downward wind blowing in the NH from the free atmosphere into the boundary layer. The latter can only be resolved with the higher vertical atmosphere model resolution (in both the coupled and uncoupled simulations). Our results support the need of resolving boundary layer entrainment of zonal momentum from the free troposphere in the WTA, which impacts strength and variability of surface winds (Stevens et al. 2002; Zermeño-Diaz and Zhang 2013; Richter et al. 2014; Meynadier et al. 2015 for EEA), as easterlies and their interannual variability are to a large extent influenced by the meridional advection and vertical mixing of zonal momentum.

TA SST variability not only is driven by wind stress but also thermodynamically (e.g. Nnamchi et al. 2015). We consider the two most important thermodynamic forcing agents, net surface shortwave radiation (SW) and latent heat flux (LH). SW is closely linked to changes in cloud cover. SW decreases almost along the entire equator and increases to the north and south of it during positive phases of the ATL3 index (Figs. 13a,b). Variability in SW is also connected to the Namibian stratocumulus region (Bellomo et al. 2015). ERA-interim and CERES_EBAF substantially differ in magnitude in the WEA and SETA. The uncoupled AGCM (Figs. S4a-c) and coupled model simulations (Fig. 13c-f) both have difficulties in simulating the SW response to ATL3 SST anomalies, especially in the SETA and partly due to large cloud cover biases. Poor simulation of marine stratocumulus cloud cover in that region is a common and long-standing problem of climate models (Ma et al. 1996; Huang and Hu 2007; Toniazzo and Woolnough 2013; Xu et al. 2014a) and unfortunately increasing atmosphere model resolution does not ameliorate the cloud bias (not shown).

The LH response to ATL3 SST anomalies constitutes a damping on the SST anomalies (negative LH is from the ocean to the atmosphere) in the EEA and SETA, whereas LH drives SST over the WEA (Figs. 14a,b). All four coupled experiments capture the basic spatial pattern, but only M-V and H-V simulate reasonable amplitude (Figs. 14c-f). It is only configuration H-V that depicts two distinct localized negative LH anomaly extremes, one in the CEA and the other in the SETA. The too strong surface wind response in the central northern TA in M-V and H-V as well as the slightly broader area of positive SST anomalies also is reflected in the LH response pattern. The two uncoupled AGCM runs L(A) and M(A) (Figs. S4d,e) overdo the response in the WEA owing to the stronger surface wind response in that region, and they miss the negative LH signal over the SETA. It is only the uncoupled AGCM experiment M-V(A) (Fig. S4f) depicting a reasonable representation of the LH response.

Elements of the Bjerknes feedback and Bjerknes index

The positive Bjerknes feedback consists of three elements. The first feedback (Figs. 15a,b), describing the relation between SST anomalies in the EEA (ATL3 region) and zonal wind stress anomalies in the WEA, is reasonably well simulated in all coupled runs (Figs. 15c-f), but experiments L and M underestimate the strength of the zonal wind stress response in the WEA. We note large biases in the off-equatorial regions in all experiments, which are not discussed here. The second feedback relates zonal wind stress anomalies in the WEA to thermocline depth anomalies represented by Z-23 anomalies (Figs. 16a,b). Anomalously strong zonal wind stress deepens (shoals) the thermocline in the west (east), thereby increasing (decreasing) zonal thermocline tilt. In contrast to the first element of the Bjerknes feedback, there are pronounced differences between the L31 and L62 configurations of the KCM, which is expected as they strongly differ in thermocline depth climatology (Fig. 6). In L and M, the Z-23 response is too weak in the WEA and in the Benguela upwelling region. M-V and H-V (Figs. 16e,f) simulate a pattern close to that calculated from ocean reanalysis data. On the downside, H-V tends to overestimate the positive Z-23 anomalies in the EEA.

Figs. 17a,b show the third Bjerknes feedback element: subsurface temperatures (represented by thermocline depth anomalies) impacting SST, termed thermocline feedback. Ocean reanalysis depict two maxima, one in the CEA and the other in the Benguela upwelling region. Interestingly, in experiments L and M the thermocline feedback is well simulated in the Benguela upwelling region but not in the CEA (Figs. 17c,d). Clearly, only M-V and H-V (Figs. 17e,f) realistically reproduce the thermocline feedback in both regions, which is probably due to the better climatological thermocline depth pattern, and also stronger cross-equatorial winds (Fig. 3) and enhanced upwelling (Fig. 7) in the EEA.

In summary, only the high-vertical resolution (L62) atmosphere model configurations of the KCM, M-V and H-V, reasonably well simulate the whole Bjerknes feedback loop, in contrast to most CMIP5 models which exhibit large biases in this respect (Deppenmeier et al. 2016). Most CMIP5 models reasonably well reproduce the first two elements of the Bjerknes feedback, despite erroneous annual cycles of SST and wind stress (as well as their variance). However, none of the CMIP5 models yields a realistic representation of the thermocline feedback (Deppenmeier et al. 2016). Chang et al. (2006) pointed to the importance of subsurface and surface coupling to amplify initial SST anomalies and trigger the positive feedback. This important link only is present in experiments M-V and H-V (Figs. S5c-d). In these coupled runs, the seasonal cycle of thermocline depth variability also is improved exhibiting a summer maximum (Fig. S3c). However, large biases remain in Z-23, with two little variability in boreal fall and early winter.

The Bjerknes Index (BJ index) is calculated for the ATL3 region from SODA (Fig. 18a) and the different configurations of the KCM. The BJ index does not necessarily well describe the feedbacks in all climate models (Graham et al. 2014), as it has been derived by assuming the recharge oscillator paradigm and because it is based on assuming linearity. Yet it is a useful tool to compare models with reanalysis data and to find differences among models. As in LMP13, the largest positive feedback in SODA is the thermocline feedback (TF). The two negative feedbacks are the dynamical and thermal damping (DD and TD, respectively), both having similar magnitude in SODA. TD relates the anomalous net surface heat flux and SST anomalies, with LH and SW contributing the most. DD is due to mean ocean currents, where mean upwelling dominates. The Ekman feedback (EF) and zonal advection feedback (ZAF) are the remaining terms and positive. EF describes how wind-induced changes in upwelling and consequently SST anomalies are related to the mean vertical temperature gradient. ZAF relates the wind-induced changes of zonal currents on SST and their impact on the zonal SST gradient. The BJ index is the sum over all terms (DD+TD+ER+ZAF+TF) and is negative for the TA. Our values calculated from SODA (Fig. 18a) correspond to those of LMP13 but slightly differ in magnitude due to different treatment of MLD, which is not further discussed here. Contrary to LMP13, we restrict our analysis to a single SODA version and use ERA40 for surface heat fluxes, since the latter was the forcing for the SODA version used here (changed to QuickSCAT winds after 2001). Hence error bars are much smaller. Ultimately, it is the relative contribution of the individual terms that is of importance.

The different KCM configurations basically yield the same relative importance of the contributing feedbacks as SODA. There is a clear distinction with regard to vertical atmosphere model resolution. In L and M (Figs. 18b,c), both damping terms are too small and the positive feedbacks of comparable size compared to SODA, and hence the BJ index (which generally is negative, representing a damped mode of variability) is smaller in magnitude. In contrast, the BJ index is three times larger in magnitude in the higher-vertical atmosphere model resolution (L62) integrations, M-V and H-V, owing to much larger negative DD and TD which are in better agreement with SODA (Figs. 18d,e). Vertical mixing of colder water dominates the DD and LH flux the TD (not shown). The positive TF also becomes larger due to a much stronger SST response to wind stress anomalies (Figs. 15e,f), higher SST sensitivity to subsurface temperature anomalies (Figs. S5c,d) and a stronger zonal thermocline tilt (Figs. 6e,f).

Seasonal analysis reveals that the BJ index can become positive in boreal spring in experiments L and M due to DD and especially TD (Fig. S6). The BJ index stays negative year round in M-V, H-V and SODA, with weakest amplitude (least stable) in summer, exactly the time of a well-developed cold tongue and largest SST variability. In SODA, this is primarily due to the large positive TF during April to June, peaking in May, one month prior to maximum SST variability in June. Especially the negative feedbacks, DD and TD, lack pronounced seasonal variation in SODA. Seasonal variability of TF is stronger in M-V and H-V, and it is more persistent and delayed by 1 to 2 months, respectively, as is the maximum SST variability in the ATL3 region (Fig. 10).

However, the BJ index analysis remains inconclusive to some extent. For example, the BJ index, counter to intuition, is larger in magnitude, i.e. more damped in experiments M-V and H-V (Fig. 18) in which the strength of interannual SST variability is reasonably well simulated. The same is true for SODA and could mean that remote forcing from e.g. the extratropical Atlantic or the Pacific would be needed to stimulate the Atlantic zonal mode.

5. Summary and discussion

We have shown that increasing atmosphere model resolution in the Kiel Climate Model (KCM), both horizontal and vertical, greatly improves simulation of the mean state and interannual variability in the tropical Atlantic (TA). The ocean component has the same coarse zonal resolution (2°) in all configurations of the KCM investigated here. In particular, the large warm SST biases in the eastern equatorial Atlantic (EEA) and southeastern tropical Atlantic

(SETA), long-standing problems in many climate models, do drastically reduce at sufficiently high horizontal and vertical atmosphere model resolution. When increasing the horizontal atmosphere model resolution, but keeping coarse vertical atmospheric resolution, the effect on the SST biases is modest. A substantial reduction of the SST biases can only be achieved when employing high vertical resolution *and* high horizontal atmosphere model resolution. The SST biases, which originally had magnitudes of up to 7 K in the Benguela upwelling region, diminish to less than 2 K. We speculate that the remaining SST biases could be, at least partly, due to the coarse horizontal ocean model resolution and insufficient low-level clouds. This study suggests that high resolution in the atmospheric component of climate models could be a key to alleviate systematic biases in the TA sector.

A major improvement is the correction of the westerly surface wind bias in boreal spring over the western equatorial Atlantic (WEA). This wind bias does not primarily have its origin in the incorrect zonal SST gradient along the equator simulated in coupled mode, since the bias also is present in companion simulations with the atmospheric component (AGCM) of the KCM, integrated in stand-alone mode with prescribed observed SSTs. This set of uncoupled AGCM experiments enables distinguishing systematic biases originating in the atmospheric component from biases due to coupling. Of the uncoupled AGCM runs, only the medium horizontal - high vertical resolution configuration M-V(A), adequately represents equatorial surface winds. This improvement is not directly related to zonal SLP, SST or precipitation gradients along the equator, but rather to a spatial redistribution of rainfall in the WEA and the transport of zonal momentum, meridional and especially vertical.

The westerly wind bias in the KCM version employing the lowest resolution (L) is strongest north of the equator and extends southward with altitude. It further coincides with deficient southerly winds that do not penetrate into the Northern Hemisphere and too weak easterlies at height. Hence, meridional transports and mixing of zonal momentum from the free troposphere into the boundary layer are too weak. Furthermore, vertical transport of zonal momentum is linked to convection that is strongest below rainfall and either missing or too weak in the case of a too southerly rainfall maximum. Vertical transport of zonal momentum also is linked to strong enough zonal winds at height. Only the KCM configurations M-V and H-V with high vertical atmosphere model resolution are able to resolve these processes and reasonably well simulate zonal wind stress in the WEA.

A correct latitudinal position of the ITCZ exhibiting a position close to the equator in boreal spring is important for the meridional winds in the EEA. They impact the onset of the cold tongue in May/June by a sudden increase of cross-equatorial winds in conjunction with the northward migration of the ITCZ and the onset of the West African Monsoon. A too southward ITCZ in the KCM configurations L and M does not allow for any seasonal SST cooling in the EEA. Improved cross-equatorial winds and rainfall north of the equator in the EEA in the higher vertical resolution configurations M-V and H-V amplify the cold tongue and support generation of significant interannual SST variability.

The large improvements in the atmospheric circulation in turn lead to major improvements in the ocean. In particular, the reduction of the westerly wind bias in the WEA and generally enhanced equatorial wind stress in the KCM versions M-V and H-V deepens (shoals) the thermocline in the western (eastern) equatorial Atlantic and enables among others cooling by cross-equatorial winds in the EEA. Subsurface temperature biases along the equator greatly ameliorate as a result of the stronger thermocline tilt, and zonal currents and upwelling along the equator become stronger. Since wave activity and other ocean dynamical processes couple the equatorial Atlantic with the SETA, pronounced improvements also occur in the SETA. However, the largest local effect in that region is due to a much narrower wind stress curl pattern and enhanced wind stress along the African coast, which is necessary to force a reasonably well meridional current pattern in the KCM configurations M, M-V and H-V. This can be achieved by increased horizontal atmosphere model resolution enabling a better resolved (convex) coastline. The enhanced vertical atmosphere model resolution strengthens alongshore wind stress and in turn meridional currents.

The low-level cloud biases over the subtropics and related radiation biases in the KCM do not significantly reduce with higher atmosphere model resolution, which emphasizes the need for refining cloud parametrization. The simulation of reasonable TA SSTs despite the presence of large low-level cloud biases at high atmosphere model resolution suggests that either the role of the cloud biases may have been overestimated in previous studies or that error compensation considerably contributed to the much improved SSTs in the KCM versions employing high atmosphere model resolution.

In the second part of this study, we show how the substantially improved climatology in the TA at higher atmosphere model resolution allows for significant interannual variability in the KCM. Seasonal phase locking of SST variability, however, only occurs at high vertical resolution in the atmospheric model component, even at low horizontal resolution. But high vertical atmosphere model resolution in conjunction with high horizontal atmosphere model resolution further improves the seasonal SST phase locking.

The complete Bjerknes feedback loop has been investigated in the different configurations of the KCM, consisting of the zonal wind stress response in the western to SST anomalies in the EEA, thermocline depth response to zonal wind stress anomalies in the WEA, and SST response to thermocline depth variability. The latter is reasonably well simulated only at sufficiently high horizontal and vertical atmosphere model resolution. Most CMIP5 models fail to reasonably well simulate all three elements of the Bjerknes feedback loop (Deppenmeier et al. 2016).

In contrast to the outstanding improvements in the mean state and interannual variability in the TA, bias reduction also occurs in the tropical Pacific (TP) but is much smaller (not shown). This is not surprising. First, biases in the TP are less severe in comparison to the TA in low atmosphere model resolution versions of the KCM. For example, the SST biases are much smaller and the SST gradient along the Pacific equator is reasonably well simulated. Second, a reasonable representation of ENSO is already present in the KCM configuration employing the lowest atmosphere model resolution. The higher sensitivity of the KCM to atmosphere model resolution in the TA compared to the TP is expected to some extent and at least partly a consequence of the unique geometry of the TA basin with its surrounding continents and the relatively small basin size.

We have shown that the seasonal phase locking of interannual SST variability correlates with the phase locking of the Bjerknes (BJ) index and to a large extent stems from the thermocline feedback destabilizing the system. This suggests that the interannual variability in the equatorial Atlantic is the result of the interaction between zonal wind stress, thermocline tilt and surface-subsurface coupling. Consequently, the simulation of zonal wind stress along the equator is of primary importance, because it largely determines the upper ocean structure in the equatorial Atlantic including thermocline tilt.

Sufficient horizontal atmosphere model resolution is essential in the Benguela upwelling region, whereby narrower coastal surface winds and more realistic ocean currents are simulated, that eventually reduce the temperature biases there. However, a large temperature bias is of equatorial origin intruding the upwelling region through wave activity (CTWs) and erroneous coastal current systems. A correct position of the ITCZ in boreal spring and summer is crucial to realistically simulate the equatorial ocean-atmosphere system as surface winds and momentum transports are tightly coupled to the rainfall band and after all establishs the upper ocean structure. Adding vertical levels in the lower atmosphere is the key to improve the position of the ITCZ. Horizontal resolution is of secondary importance in that regard.

We have shown that it is possible with the KCM system to reasonably well simulate the climatology and the interannual variability in the TA with a coarse-resolution ocean model when employing high atmosphere model resolution. The much better represented mean ocean state, seasonal and qinterannual variability when using high atmosphere model resolution is primarily the result of the improvement in the atmosphere model itself. In contrast, a coupled model with high oceanic resolution but low atmospheric resolution would not necessarily result in a similar improvement in the KCM system. This is because of intrinsic errors in the atmosphere model at coarse resolution, which has been demonstrated by companion experiments with the AGCM forced by observed SSTs. We argue that increasing the oceanic resolution is of lesser importance, since the ocean model even at a relatively coarse resolution adequately responds to wind stress variability and resolves most processes required to simulate the climatology and interannual variability in the TA. Nevertheless, we hypothesize that coupled models will benefit from higher resolution in both model components, as substantial surface and subsurface biases remain. Resolving mesoscale and submesoscale structures like eddies and filaments forming at the front between the cold upwelled water and the warm surface water in the Benguela upwelling region, for example, may help to further reduce warm SST biases in the SETA and will be highly important for other applications like biogeochemical and ecosystem modeling.

Acknowledgements

We thank two anonymous reviewers for their thoughtful comments. This work was supported by the Bundesministerium für Bildung und Forschung grant SACUS (03G0837A) and EU FP7/2007-2013 under grant agreement no. 603521, project PREFACE. Model integrations were performed at the Norddeutscher Verbund für Hoch- und Höchstleistungsrechnen and the Rechenzentrum der Universität Kiel.

References

Adler RF, Huffman GJ, Chang A, et al (2003) The Version-2 Global Precipitation Climatology Project (GPCP) Monthly Precipitation Analysis (1979–Present). J Hydrometeorol 4:1147–1167. doi: 10.1175/1525-7541(2003)004<1147:TVGPCP>2.0.CO;2

Ashfaq M, Skinner CB, Diffenbaugh NS (2011) Influence of SST biases on future climate change projections. Clim Dyn 36:1303–1319. doi: 10.1007/s00382-010-0875-2

Bachèlery M-L, Illig S, Dadou I (2015) Interannual variability in the South-East Atlantic Ocean, focusing on the Benguela Upwelling System: Remote versus local forcing. J Geophys Res Ocean n/a-n/a. doi: 10.1002/2015JC011168

Bellomo K, Clement AC, Mauritsen T, et al (2015) The Influence of Cloud Feedbacks on Equatorial Atlantic Variability. J Clim 28:2725–2744. doi: 10.1175/JCLI-D-14-00495.1

Biasutti M, Sobel AH, Kushnir Y (2006) AGCM Precipitation Biases in the Tropical Atlantic. J Clim 19:935–958. doi: 10.1175/JCLI3673.1

Brandt P, Funk A, Hormann V, et al (2011) Interannual atmospheric variability forced by the deep equatorial Atlantic Ocean. Nature 473:497–500. doi: 10.1038/nature10013

Breugem W-P, Hazeleger W, Haarsma RJ (2006) Multimodel study of tropical Atlantic variability and change. Geophys Res Lett 33:1–5. doi: 10.1029/2006GL027831

Caniaux G, Giordani H, Redelsperger J-L, et al (2011) Coupling between the Atlantic cold tongue and the West African monsoon in boreal spring and summer. J Geophys Res 116:C04003. doi: 10.1029/2010JC006570

Carton JA, Giese BS (2008) A Reanalysis of Ocean Climate Using Simple Ocean Data Assimilation (SODA). Mon Weather Rev 136:2999–3017. doi: 10.1175/2007MWR1978.1

Chang C-Y, Carton J a., Grodsky S a., Nigam S (2007) Seasonal Climate of the Tropical Atlantic Sector in the NCAR Community Climate System Model 3: Error Structure and Probable Causes of Errors. J Clim 20:1053–1070. doi: 10.1175/JCLI4047.1

Chang C-Y, Nigam S, Carton J a. (2008) Origin of the Springtime Westerly Bias in Equatorial Atlantic Surface Winds in the Community Atmosphere Model Version 3 (CAM3) Simulation. J Clim 21:4766–4778. doi: 10.1175/2008JCLI2138.1

Chang P, Yamagata T, Schopf P, et al (2006) Climate Fluctuations of Tropical Coupled Systems—The Role of Ocean Dynamics. J Clim 19:5122–5174. doi: 10.1175/JCLI3903.1

Compo GP, Whitaker JS, Sardeshmukh PD, et al (2011) The Twentieth Century Reanalysis Project. Q J R Meteorol Soc 137:1–28. doi: 10.1002/qj.776

Davey M, Huddleston M, Sperber K, et al (2002) STOIC: a study of coupled model climatology and variability in tropical ocean regions. Clim Dyn 18:403–420. doi: 10.1007/s00382-001-0188-6

Dee DP, Uppala SM, Simmons a. J, et al (2011) The ERA-Interim reanalysis: configuration and performance of the data assimilation system. Q J R Meteorol Soc 137:553–597. doi: 10.1002/qj.828

Delworth TL, Rosati A, Anderson W, et al (2012) Simulated Climate and Climate Change in the GFDL CM2.5 High-Resolution Coupled Climate Model. J Clim 25:2755–2781. doi: 10.1175/JCLI-D-11-00316.1

Deppenmeier A-L, Haarsma RJ, Hazeleger W (2016) The Bjerknes feedback in the tropical Atlantic in CMIP5 models. Clim Dyn 47:2691–2707. doi: 10.1007/s00382-016-2992-z

Deser C, Capotondi A, Saravanan R, Phillips AS (2006) Tropical Pacific and Atlantic Climate Variability in CCSM3. J Clim 19:2451–2481. doi: 10.1175/JCLI3759.1

DeWitt DG (2005) Diagnosis of the tropical Atlantic near-equatorial SST bias in a directly coupled atmosphere-ocean general circulation model. Geophys Res Lett 32:1–4. doi: 10.1029/2004GL021707

Ding H, Greatbatch RJ, Latif M, Park W (2015a) The impact of sea surface temperature bias on equatorial Atlantic interannual variability in partially coupled model experiments. Geophys Res Lett 42:5540–5546. doi: 10.1002/2015GL064799

Ding H, Keenlyside N, Latif M, et al (2015b) The impact of mean state errors on equatorial Atlantic interannual variability in a climate model. J Geophys Res Ocean 120:1133–1151. doi: 10.1002/2014JC010384

Doi T, Tozuka T, Sasaki H, et al (2007) Seasonal and Interannual Variations of Oceanic Conditions in the Angola Dome. J Phys Oceanogr 37:2698–2713. doi: 10.1175/2007JPO3552.1

Doi T, Vecchi G a., Rosati AJ, Delworth TL (2012) Biases in the Atlantic ITCZ in Seasonal–Interannual Variations for a Coarse- and a High-Resolution Coupled Climate Model. J Clim 25:5494–5511. doi: 10.1175/JCLI-D-11-00360.1

Florenchie P, Reason CJC, Lutjeharms JRE, et al (2004) Evolution of Interannual Warm and Cold Events in the Southeast Atlantic Ocean. J Clim 17:2318–2334. doi: 10.1175/1520-0442(2004)017<2318:EOIWAC>2.0.CO;2

Giannini A, Saravanan R, Chang P (2003) Oceanic Forcing of Sahel Rainfall on Interannual to Interdecadal Time Scales. Science (80-) 302:1027–1030. doi: 10.1126/science.1089357

Graham FS, Brown JN, Langlais C, et al (2014) Effectiveness of the Bjerknes stability index in representing ocean dynamics. Clim Dyn 43:2399–2414. doi: 10.1007/s00382-014-2062-3

Guinehut S, Coatanoan C, Dhomps A-L, et al (2009) On the Use of Satellite Altimeter Data in Argo Quality Control. J Atmos Ocean Technol 26:395–402. doi: 10.1175/2008JTECHO648.1

Hagemann S, Arpe K, Roeckner E (2006) Evaluation of the Hydrological Cycle in the ECHAM5 Model. J Clim 19:3810–3827. doi: 10.1175/JCLI3831.1

Harlaß J, Latif M, Park W (2015) Improving climate model simulation of tropical Atlantic sea surface temperature: The importance of enhanced vertical atmosphere model resolution. Geophys Res Lett 42:2401–2408. doi: 10.1002/2015GL063310

Hormann V, Brandt P (2009) Upper equatorial Atlantic variability during 2002 and 2005 associated with equatorial Kelvin waves. J Geophys Res 114:C03007. doi: 10.1029/2008JC005101

Hourdin F, Găinuşă-Bogdan A, Braconnot P, et al (2015) Air moisture control on ocean surface temperature, hidden key to the warm bias enigma. Geophys Res Lett 41:n/a-n/a. doi: 10.1002/2015GL066764

Huang B, Hu Z-Z (2007) Cloud-SST feedback in southeastern tropical Atlantic anomalous events. J Geophys Res 112:1–19. doi: 10.1029/2006JC003626

Huang B, Hu ZZ, Jha B (2007) Evolution of model systematic errors in the tropical atlantic basin from coupled climate hindcasts. Clim Dyn 28:661–682. doi: 10.1007/s00382-006-0223-8

Huffman GJ, Bolvin DT, Nelkin EJ, et al (2007) The TRMM Multisatellite Precipitation Analysis (TMPA): Quasi-Global, Multiyear, Combined-Sensor Precipitation Estimates at Fine Scales. J Hydrometeorol 8:38–55. doi: 10.1175/JHM560.1

Jin F-F, Kim ST, Bejarano L (2006) A coupled-stability index for ENSO. Geophys Res Lett 33:L23708. doi: 10.1029/2006GL027221

Kato S, Loeb NG, Rose FG, et al (2013) Surface Irradiances Consistent with CERES-Derived Top-of-Atmosphere Shortwave and Longwave Irradiances. J Clim 26:2719–2740. doi: 10.1175/JCLI-D-12-00436.1

Keenlyside N, Latif M (2007) Understanding Equatorial Atlantic Interannual Variability. J Clim 20:131–142. doi: 10.1175/JCLI3992.1

Krebs M, Biastoch A, Böning CW, Latif M (2017) Understanding Benguela Upwelling System Warm Sea Surface Temperature Bias in a Forced Ocean Model.

Large WG, Danabasoglu G (2006) Attribution and Impacts of Upper-Ocean Biases in CCSM3. J Clim 19:2325–2346. doi: 10.1175/JCLI3740.1

Li G, Xie S-P (2012) Origins of tropical-wide SST biases in CMIP multi-model ensembles. Geophys Res Lett 39:n/a-n/a. doi: 10.1029/2012GL053777

Lübbecke JF, Böning CW, Keenlyside N, Xie S-P (2010) On the connection between Benguela and equatorial Atlantic Niños and the role of the South Atlantic Anticyclone. J Geophys Res 115:C09015. doi: 10.1029/2009JC005964

Lübbecke JF, McPhaden MJ (2013) A Comparative Stability Analysis of Atlantic and Pacific Niño Modes*. J Clim 26:5965–5980. doi: 10.1175/JCLI-D-12-00758.1

Ma C-C, Mechoso CR, Robertson AW, Arakawa A (1996) Peruvian Stratus Clouds and the Tropical Pacific Circulation: A Coupled Ocean-Atmosphere GCM Study. J Clim 9:1635–1645. doi: 10.1175/1520-0442(1996)009<1635:PSCATT>2.0.CO;2

Madec G (2008) NEMO ocean engine. Note du Pole de modelisation, Institut Pierre-Simon Laplace (IPSL) No 27, France

Meynadier R, de Coëtlogon G, Leduc-Leballeur M, et al (2015) Seasonal influence of the sea surface temperature on the low atmospheric circulation and precipitation in the eastern equatorial Atlantic. Clim Dyn. doi: 10.1007/s00382-015-2892-7

Mitchell TP, Wallace JM (1992) The Annual Cycle in Equatorial Convection and Sea Surface Temperature. J Clim 5:1140–1156. doi: 10.1175/1520-0442(1992)005<1140:TACIEC>2.0.CO;2

Nnamchi HC, Li J, Kucharski F, et al (2015) Thermodynamic controls of the Atlantic Niño. Nat Commun 6:8895. doi: 10.1038/ncomms9895

Okumura YM, Xie S-P (2004) Interaction of the Atlantic Equatorial Cold Tongue and the African Monsoon*. J Clim 17:3589–3602. doi: 10.1175/1520-0442(2004)017<3589:IOTAEC>2.0.CO;2

Park W, Keenlyside N, Latif M, et al (2009) Tropical Pacific Climate and Its Response to Global Warming in the Kiel Climate Model. J Clim 22:71–92. doi: 10.1175/2008JCLI2261.1

Patricola CM, Chang P (2016) Structure and dynamics of the Benguela low-level coastal jet. Clim Dyn 0:0. doi: 10.1007/s00382-016-3479-7

Patricola CM, Li M, Xu Z, et al (2012) An investigation of tropical Atlantic bias in a high-resolution coupled regional climate model. Clim Dyn 39:2443–2463. doi: 10.1007/s00382-012-1320-5

Philander SGH, Pacanowski RC (1981) The oceanic response to cross-equatorial winds (with application to coastal upwelling in low latitudes). Tellus 33:201–210. doi: 10.1111/j.2153-3490.1981.tb01744.x

Polo I, Lazar A, Rodriguez-Fonseca B, Arnault S (2008) Oceanic Kelvin waves and tropical Atlantic intraseasonal variability: 1. Kelvin wave characterization. J Geophys Res 113:C07009. doi: 10.1029/2007JC004495

Rayner NA (2003) Global analyses of sea surface temperature, sea ice, and night marine air temperature since the late nineteenth century. J Geophys Res 108:4407. doi: 10.1029/2002JD002670

Repelli CA, Nobre P (2004) Statistical prediction of sea-surface temperature over the tropical Atlantic. Int J Climatol 24:45–55. doi: 10.1002/joc.982

Reynolds RW (2009) What's New in Version 2. http://www.ncdc.noaa.gov/sites/default/files/attachments/Reynolds2009_oisst_daily_v02r00_version2-features.pdf. Accessed 3 Mar 2016

Reynolds RW, Smith TM, Liu C, et al (2007) Daily High-Resolution-Blended Analyses for Sea Surface Temperature. J Clim 20:5473–5496. doi: 10.1175/2007JCLI1824.1

Richter I, Behera SK, Doi T, et al (2014) What controls equatorial Atlantic winds in boreal spring? Clim Dyn 43:3091–3104. doi: 10.1007/s00382-014-2170-0

Richter I, Xie S-P (2008) On the origin of equatorial Atlantic biases in coupled general circulation models. Clim Dyn 31:587–598. doi: 10.1007/s00382-008-0364-z

Richter I, Xie S-P, Behera SK, et al (2012) Equatorial Atlantic variability and its relation to mean state biases in CMIP5. Clim Dyn 42:171–188. doi: 10.1007/s00382-012-1624-5

Richter I, Xie S-P, Wittenberg AT, Masumoto Y (2011) Tropical Atlantic biases and their relation to surface wind stress and terrestrial precipitation. Clim Dyn 38:985–1001. doi: 10.1007/s00382-011-1038-9

Risien CM, Chelton DB (2008) A Global Climatology of Surface Wind and Wind Stress Fields from Eight Years of QuikSCAT Scatterometer Data. J Phys Oceanogr 38:2379–2413. doi: 10.1175/2008JPO3881.1

Roeckner E, Baeuml G, Bonventura L, et al (2003) The atmospheric general circulation model ECHAM5. PART I: Model description, Report 349. Max Planck Institute for Meteorology, Hamburg, Germany

Servain J, Picaut J, Merle J (1982) Evidence of Remote Forcing in the Equatorial Atlantic Ocean. J Phys Oceanogr 12:457–463. doi: 10.1175/1520-0485(1982)012<0457:EORFIT>2.0.CO;2

Small RJ, Bacmeister J, Bailey D, et al (2014) A new synoptic-scale resolving global climate simulation using the Community Earth System Model. J Adv Model Earth Syst 6:1065–1094. doi: 10.1002/2014MS000363

Small RJ, Curchitser E, Hedstrom K, et al (2015) The Benguela Upwelling System: Quantifying the Sensitivity to Resolution and Coastal Wind Representation in a Global Climate Model*. J Clim 28:9409–9432. doi: 10.1175/JCLI-D-15-0192.1

Steinig S, Latif M, Harlaß J, Park W (2016) Sensitivity of West African Monsoon and Sahel Rainfall to resolution.

Stevens B, Duan J, McWilliams JC, et al (2002) Entrainment, Rayleigh Friction, and Boundary Layer Winds over the Tropical Pacific. J Clim 15:30–44. doi: 10.1175/1520-0442(2002)015<0030:ERFABL>2.0.CO;2

Stockdale TN, Balmaseda M a., Vidard A (2006) Tropical Atlantic SST prediction with coupled ocean-atmosphere GCMs. J Clim 19:6047–6061. doi: 10.1175/JCLI3947.1

Taylor KE, Stouffer RJ, Meehl GA (2012) An Overview of CMIP5 and the Experiment Design. Bull Am Meteorol Soc 93:485–498. doi: 10.1175/BAMS-D-11-00094.1

Toniazzo T, Woolnough S (2013) Development of warm SST errors in the southern tropical Atlantic in CMIP5 decadal hindcasts. Clim Dyn 43:28889–2913. doi: 10.1007/s00382-013-1691-2

Tozuka T, Doi T, Miyasaka T, et al (2011) Key factors in simulating the equatorial Atlantic zonal sea surface temperature gradient in a coupled general circulation model. J Geophys Res 116:1–12. doi: 10.1029/2010JC006717

Uppala SM, Kaallberg PW, Simmons AJ, et al (2005) The ERA-40 re-analysis. Q J R Meteorol Soc 131:2961–3012. doi: 10.1256/qj.04.176

Voldoire A, Claudon M, Caniaux G, et al (2014) Are atmospheric biases responsible for the tropical Atlantic SST biases in the CNRM-CM5 coupled model? Clim Dyn 43:2963–2984. doi: 10.1007/s00382-013-2036-x

Wahl S, Latif M, Park W, Keenlyside N (2011) On the Tropical Atlantic SST warm bias in the Kiel Climate Model. Clim Dyn 36:891–906. doi: 10.1007/s00382-009-0690-9

Wan X, Chang P, Jackson CS, et al (2011) Plausible effect of climate model bias on abrupt climate change simulations in Atlantic sector. Deep Sea Res Part II Top Stud Oceanogr 58:1904–1913. doi: 10.1016/j.dsr2.2010.10.068

Wentz FJ, Scott J, Hoffman R, et al (2015) Remote Sensing Systems Cross-Calibrated Multi-Platform (CCMP) 6-hourly ocean vector wind analysis product on 0.25 deg grid, Version 2.0. Remote Sensing Systems, Santa Rosa, CA.

Xie S-P (1994) On the Genesis of the Equatorial Annual Cycle. J Clim 7:2008–2013. doi: 10.1175/1520-0442(1994)007<2008:OTGOTE>2.0.CO;2

Xie S-P, Carton JA (2004) Tropical Atlantic variability: Patterns, mechanisms, and impacts. In: Wang C, Xie S-P, Carton JA (eds) Earth Climate: The Ocean-Atmosphere Interaction. Geophysical Monograph, AGU, Washington, D.C, pp 121–142

Xu Z, Chang P, Richter I, et al (2014a) Diagnosing southeast tropical Atlantic SST and ocean circulation biases in the CMIP5 ensemble. Clim Dyn 43:3123–3145. doi: 10.1007/s00382-014-2247-9

Xu Z, Li M, Patricola CM, Chang P (2014b) Oceanic origin of southeast tropical Atlantic biases. Clim Dyn 43:2915–2930. doi: 10.1007/s00382-013-1901-y

Yu L, Jin X, Weller RA (2008) Multidecade Global Flux Datasets from the Objectively Analyzed Air-sea Fluxes (OAFlux) Project: Latent and sensible heat fluxes, ocean evaporation, and related surface meteorological variables. Woods Hole Oceanographic Institution, OAFlux Project Technical Report. OA-2008-01, 64pp. Woods Hole. Massachusetts.

Zermeño-Diaz DM, Zhang C (2013) Possible Root Causes of Surface Westerly Biases over the Equatorial Atlantic in Global Climate Models. J Clim 26:8154–8168. doi: 10.1175/JCLI-D-12-00226.1

Figure Captions

Fig. 1 March-April-May mean SST bias (shading, °C) w.r.t NOAA-OISST, mean total precipitation (contours, interval 2 mm/day), mean 10m wind (vectors, m/s). a) Observed mean state in SST (NOAA-OISST), total precipitation (GPCP2) and 10m winds (ERA-interim), all 1982-2009, b) CMIP5 historical multi model ensemble mean, c) T42 L31 (L), d) T159 L31 (M), e) T159 L62 (M-V), f) T255 L62 (H-V)

Fig. 2 As Fig. 1, but for July-August-September (JAS) means

Fig. 3 Seasonal cycle of zonally averaged (10°W-0°W) total precipitation (contours, interval 2 mm/day) and 10m wind vectors (shading denotes magnitude in m/s) over latitude. a) GPCP2.2 and ERA-interim (both 1982-2009), b) TRMM 3B43 (1998-2014) and CCMP2 (1988-2014), c) T42 L31 (L), d) T159 L31 (M), e) T159 L62 (M-V), f) T255 L62 (H-V)

Fig. 4 Latitude-height section of mean winds (m/s) and total rainfall (red line, mm/day) in March-April-May (MAM) averaged over 40°W-10°W. Shading denotes zonal wind, vectors meridional-vertical wind (vertical wind scaled by 90), thick red lines represent particular model output and thick black line denotes observed TRMM rainfall in a) and GPCP2.2 in b)-f). a) ERA-interim wind (1982-2009) and TRMM rainfall (1988-2014), b) 20CRv2 winds and GPCP2.2 rainfall (both 1982-2009), c) T42 L31 (L), d) T159 L31 (M), e) T159 L62 (M-V), f) T255 L62 (H-V)

Fig. 5 Lines denote green: T42 L31 (L/L(A)), red: T159 L31 (M/M(A)), blue: T159 L62 (M-V/M-V(A)), purple: T255 L62 (H-V), black crossed: observations. a) 10m zonal wind (m/s) in WTA (40°W-10°W, 3°S-3°N) for coupled models and b) for uncoupled models, obs: ERA-interim, c) SLP gradient (hPa) for coupled model and d) for uncoupled model, obs: ERA-interim, e) total precipitation gradient (same boxes, mm/day) for coupled model and f) for uncoupled model, obs: GPCP2.2, g) SST gradient (°C) for coupled model, obs: NOAA-OISST, h) SST w.r.t. annual mean (°C) in ATL3 (20°W-0°W, 3°S-3°N) for coupled model, obs: NOAA-OISST. WTA: 40°W-10°W, 3°S-3°N. Zonal E - W gradient as the difference between 10°W-10°E – 50°W-40°W at 3°S-3°N.

Fig. 6 Hovmöller diagram of 23°C isotherm (shading, m) and wind stress (vectors, Pa) averaged over 3°S-3°N. a) SODA (1958-2001), b) HadEN3 (1955-2010) isotherm, ERA-interim (1982-2009) wind stress, c) T42 L31 (L), d) T159 L31 (M), e) T159 L62 (M-V), f) T255 L62 (H-V)

Fig. 7 Depth-Longitude section along the equator (3°S-3°N) in MAM. Mean temperature bias (w.r.t SODA, shading, °C), mean vertical velocity (vectors, cm/day) and mean zonal currents, contours, interval 2, 4, 6, 8, 10, 15, 20, 25, 30, 35, 40 cm/s, dashed negative (westward). a) T42 L31 (L), b) T159 L31 (M), c) T159 L62 (M-V), d) T255 L62 (H-V), e) SODA (1958-2001)

Fig. 8 JAS mean Depth-Latitude section along the African coast for mean temperature bias (w.r.t SODA, shading, °C, 4°-longitude-band) and mean vertical velocity (vectors, cm/day, 2°-longitude-band). a) T42 L31 (L), b) T159 L31 (M),

c) T159 L62 (M-V), d) T255 L62 (H-V), e) T42 L31 (L) for AMJ, f) mean temperature and vertical velocity in SODA (1958-2001) for a 1° longitude-band.

Fig. 9 JAS mean wind stress (vectors, N/m^2) and curl (shading, N/m^{3}x10e^6) in a-g), depth integrated meridional currents (cm/s, upper 15-216m) in h-l) and SST anomalies (K, w.r.t. global mean) in m-q). a) QuikSCAT (1999-2009), b) ERA-interim (1982-2009), c+g) SODA (1958-2001), d+i+n) T42 L31 (L), e+j+o) T159 L31 (M), f+k+p) T159 L62 (M-V), g+l+q) T255 L62 (H-V)

Fig. 10 Monthly stratified standard deviation of SST anomalies (°C) in the ATL3 region (20°W-0°W, 3°S-3°N). Black cross denotes NOAA-OISST (1982-2009), green: T42 L31 (L), red: T159 L31 (M), blue: T159 L62 (MV), purple: T255 L62 (H-V)

Fig. 11 Regression of 10m wind (vectors, m/s per °C) and total precipitation anomalies (shading, mm/day per °C) on ATL3 SST anomalies. Stippling denotes 95% significance level, and only significant vectors depicted. a) HadISST, ERA-interim and GPCP2 (all 1982-2009), b) NOAA-OISST and 20CRv2 (both 1982-2009), c) T42 L31 (L), d), T159 L31 (M), e) T159 L62 (M-V), f) T255 L62 (H-V).

Fig. 12 Regression of 3-dimensional wind field on ATL3 SST in m/s per °C as Latitude-Height section at 40°W. Zonal wind response shaded, meridional and vertical wind response as vectors. Vertical wind scaled by 60. Stippling denotes 95% significance level, only significant vectors depicted. a) T42 L31 L(A), b), T159 L31 M(A), c) T159 L62 M-V(A), d) HadISST and ERA-interim (both 1982-2009), e) T42 L31 (L), f), T159 L31 (M), g) T159 L62 (M-V), h) T255 L62 (H-V)

Fig. 13 Regression of net surface short wave radiation (SW) anomalies on ATL3 SST anomalies (W/m^2 per °C). Stippling denotes 95% significance level. a) HadISST and CERES EBAF (both 2001-2015), b) NOAA-OISST and ERA-interim (both 1982-2009), c) T42 L31 (L), d) T159 L31 (M), e) T159 L62 (M-V), f) T255 L62 (H-V)

Fig. 14 Regression of latent heat (LH) flux anomalies (W/m^2 per °C) on ATL3 SST anomalies. Stippling denotes 95% significance level. a) HadISST and ERA-interim (both 1982-2009), b) NOAA-OISST and OAFlux (both 1984-2009), c) T42 L31 (L), d), T159 L31 (M), e) T159 L62 (M-V), f) T255 L62 (H-V)

Fig. 15 1st Bjerknes feedback component: regression of wind stress on ATL3 SST (Pa*100/°C). Stippling denotes 95% significance level. a) HadISST and ERA-interim (both 1982-2009), b) SODA (1958-2001), c) T42 L31 (L), d) T159 L31 (M), e) T159 L62 (M-V), f) T255 L62 (H-V)

Fig. 16 2nd Bjerknes feedback component: regression of 23°C isotherm depth on wind stress (m/Pa*100) in the WA3 region (3°S-3°N, 40°W-20°W). Stippling denotes 95% significance level. a) SODA (1958-2001), b) ERA-interim and HadEN3 (both 1982-2009), c) T42 L31 (L), d) T159 L31 (M), e) T159 L62 (M-V), f) T255 L62 (H-V)

Fig. 17 3rd Bjerknes feedback component: regression of SST on 23°C isotherm depth (°C/10m) in ATL3 (3°S-3°N, 20°W-0°W). Stippling denotes 95% significance level. a) SODA (1958-2001), b) HadISST and HadEN3 (both 1982-2009), c) T42 L31 (L), d) T159 L31 (M), e) T159 L62 (M-V), f) T255 L62 (H-V)

Fig. 18 Bjerknes index components and total Bjerknes index. a) SODA and ERA40 (both 1958-2001), b) T42 L31 (L), c) T159 L31 (M), d) T159 L62 (M-V), e) T255 L62 (H-V). DD – Dynamical damping (green), TD – Thermal damping (turquoise), ZAF – Zonal advection feedback (magenta), EF – Ekman feedback (yellow), TF – Thermocline feedback (red), Bjerknes index as sum over all feedbacks (blue). See section 2 for calculation procedure.

Supplementary Figures

Fig. S1 Regression of SST on ATL3 SST anomalies (°C/°C). Stippling denotes 95% significance level. a) HadISST (1982-2009), b) NOAA-OISST (1982-2009), c) T42 L31 (L), d) T159 L31 (M), e) T159 L62 (M-V), f) T255 L62 (H-V)

Fig. S2 Regression of 10m winds (vectors, m/s per °C) and total precipitation (shading, mm/day per °C) on ATL3 SST for uncoupled simulations. Stippling denotes 95% significance level, only significant vectors depicted. a) T42 L31 L(A), b) T159 L31 M(A), c) T159 L62 M-V(A)

Fig. S3 Lines denote green: T42 L31 (L/L(A)), red: T159 L31 (M/M(A)), blue: T159 L62 (M-V/M-V(A)), purple: T255 L62 (H-V), black crossed: observations. a) zonal wind at 850hPa (m/s) in WTA (40°W-10°W, 3°S-3°N) for coupled models and b) for uncoupled models, obs: ERA-interim, c) standard deviation (STD) of 23°C isotherm depth in ATL3 (20°W-0°W, 3°S-3°N) for coupled models, obs: SODA.

Fig. S4 Regression of net surface short wave radiation (SW, a-c) and latent heat flux (LH, d-f) anomalies on ATL3 SST anomalies (W/m^2 per °C) for uncoupled simulations a/d) T42 L31 L(A), b/e) T159 L31 M(A), c/f) T159 L62 M-V(A). . Stippling denotes 95% significance level.

Fig. S5 Regression of upper ocean temperature (averaged over 3°S-3°N) on ATL3 SST (°C/°C). Stippling denotes 95% significance level. a) T42 L31 (L), b) T159 L31 (M), c) T159 L62 (M-V), d) T255 L62 (H-V), e) SODA (1958-2001)

Fig. S6 Seasonally stratified Bjerknes index. Abbreviations are as in Fig. 18. Lines denote: black crossed: SODA (1958-2001), green: T42 L31 (L), red: T159 L31 (M), blue: T159 L62 (M-V), purple: T255 L62 (H-V)

Figure 1

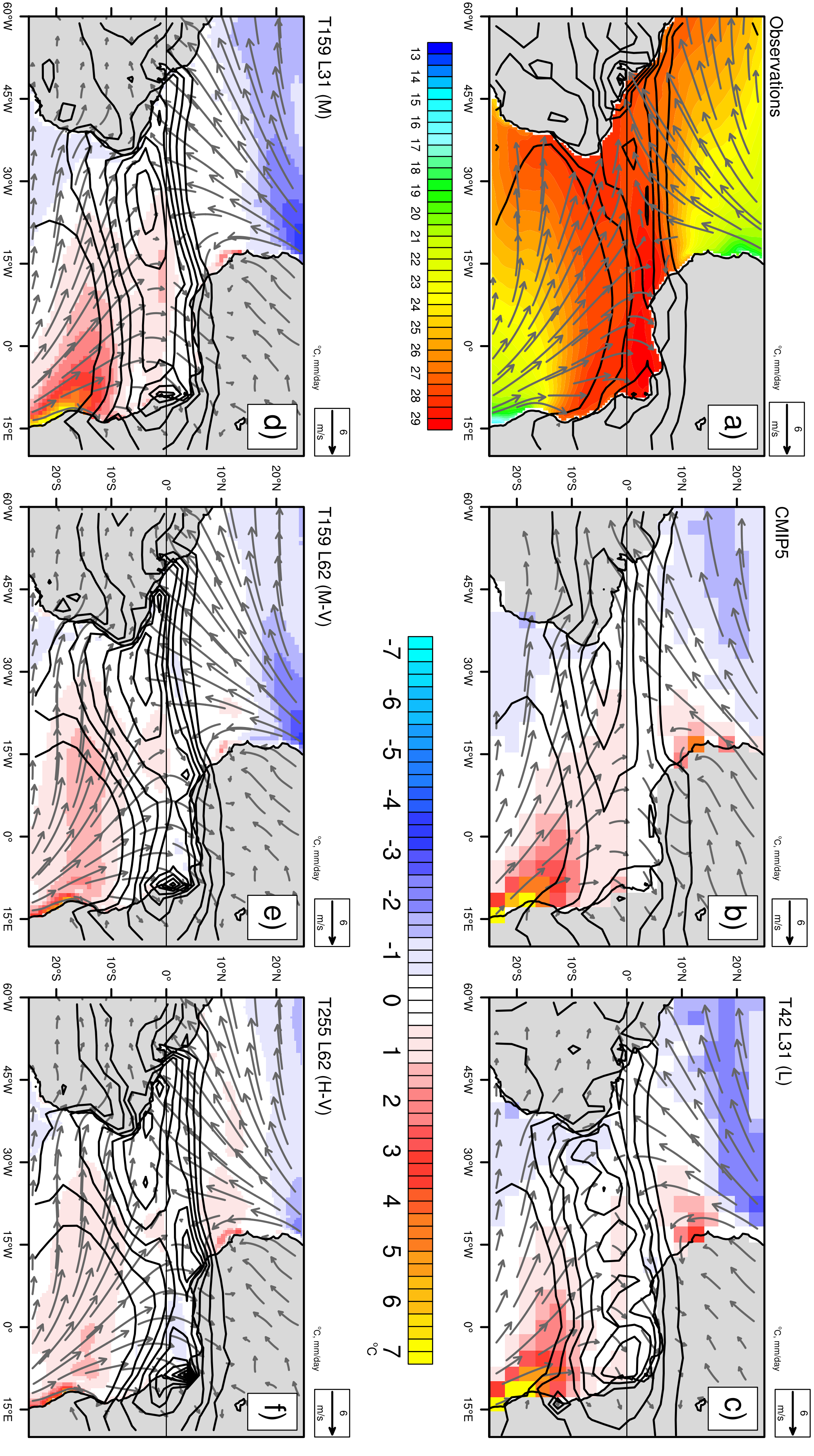

Observations
a)
CMIP5
b)
T42 L31 (L)
c)
T159 L31 (M)
d)
T159 L62 (M-V)
e)
T255 L62 (H-V)
f)
6
m/s
°C, mm/day
20°N
10°N
0°
10°S
20°S
60°W
45°W
30°W
15°W
0°
15°E
13
14
15
16
17
18
19
20
21
22
23
24
25
26
27
28
29
-7
-6
-5
-4
-3
-2
-1
0
1
2
3
4
5
6
7
°C

Figure 2

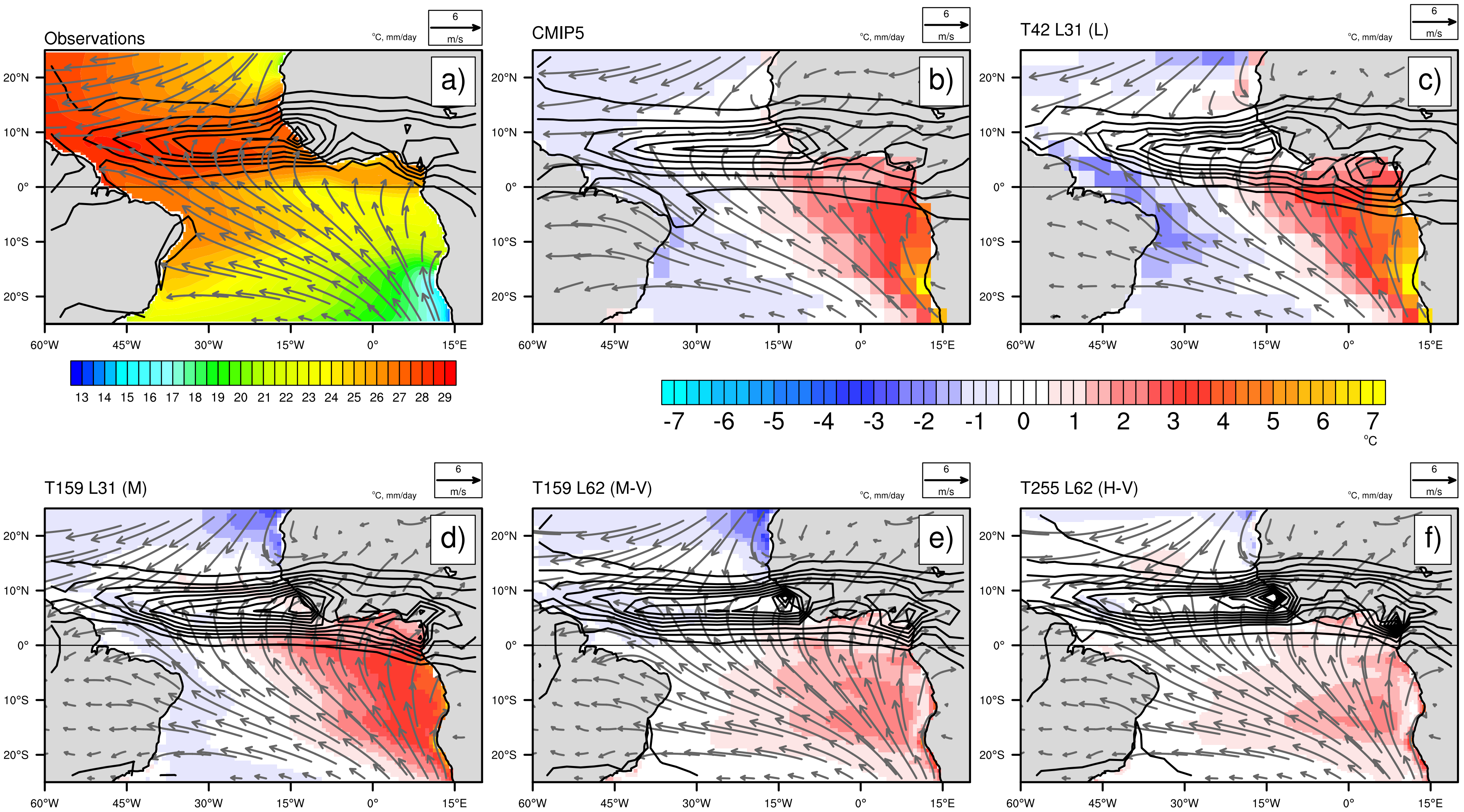
Observations
CMIP5
T42 L31 (L)
T159 L31 (M)
T159 L62 (M-V)
T255 L62 (H-V)
a)
b)
c)
d)
e)
f)
°C, mm/day
6
m/s
20°N
10°N
0°
10°S
20°S
60°W
45°W
30°W
15°W
0°
15°E
13 14 15 16 17 18 19 20 21 22 23 24 25 26 27 28 29
-7 -6 -5 -4 -3 -2 -1 0 1 2 3 4 5 6 7
°C

Figure 3

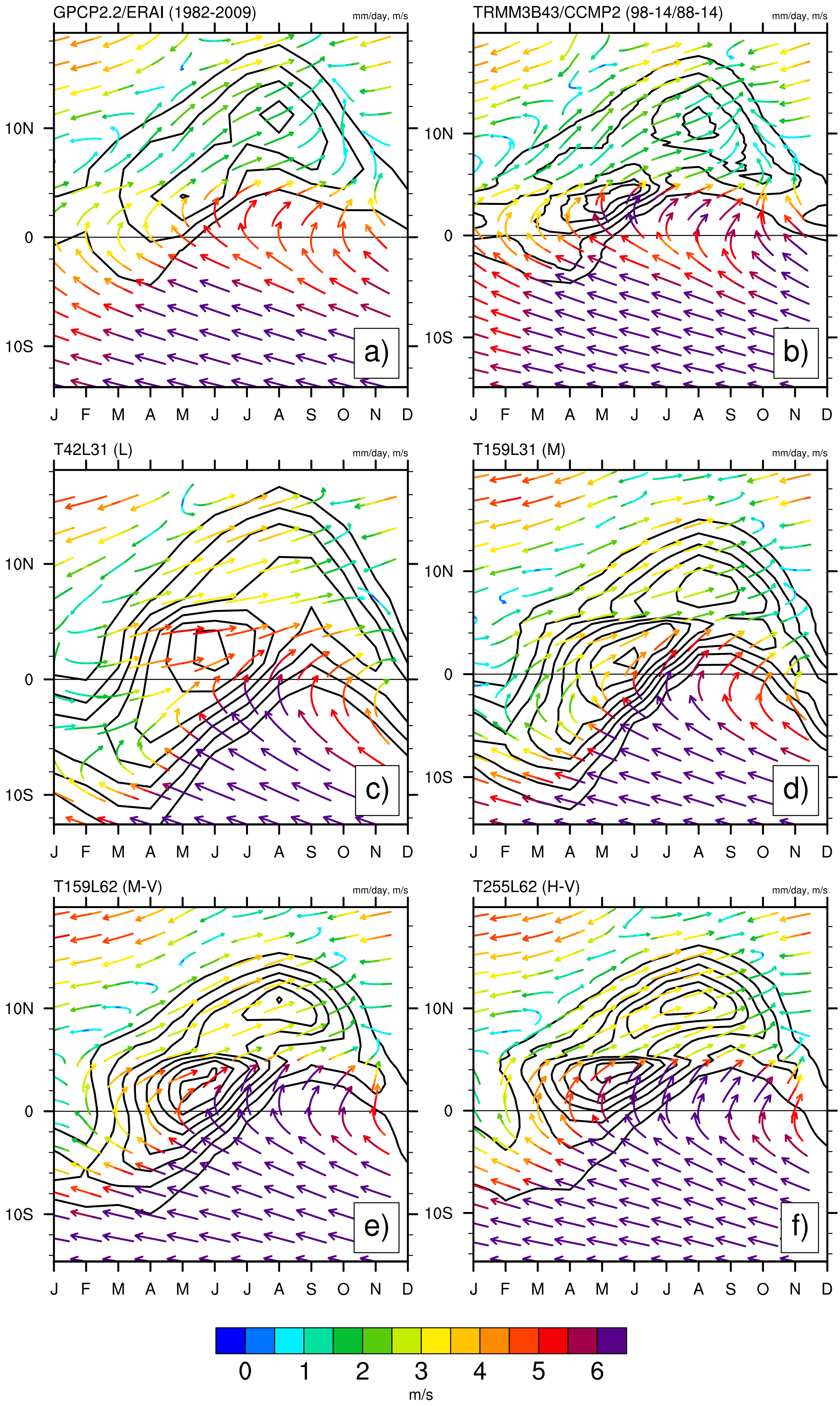
GPCP2.2/ERAI (1982-2009)
mm/day, m/s
TRMM3B43/CCMP2 (98-14/88-14)
mm/day, m/s
T42L31 (L)
mm/day, m/s
T159L31 (M)
mm/day, m/s
T159L62 (M-V)
mm/day, m/s
T255L62 (H-V)
mm/day, m/s
10N
0
10S
J F M A M J J A S O N D
a)
b)
c)
d)
e)
f)
0 1 2 3 4 5 6
m/s

Figure 4

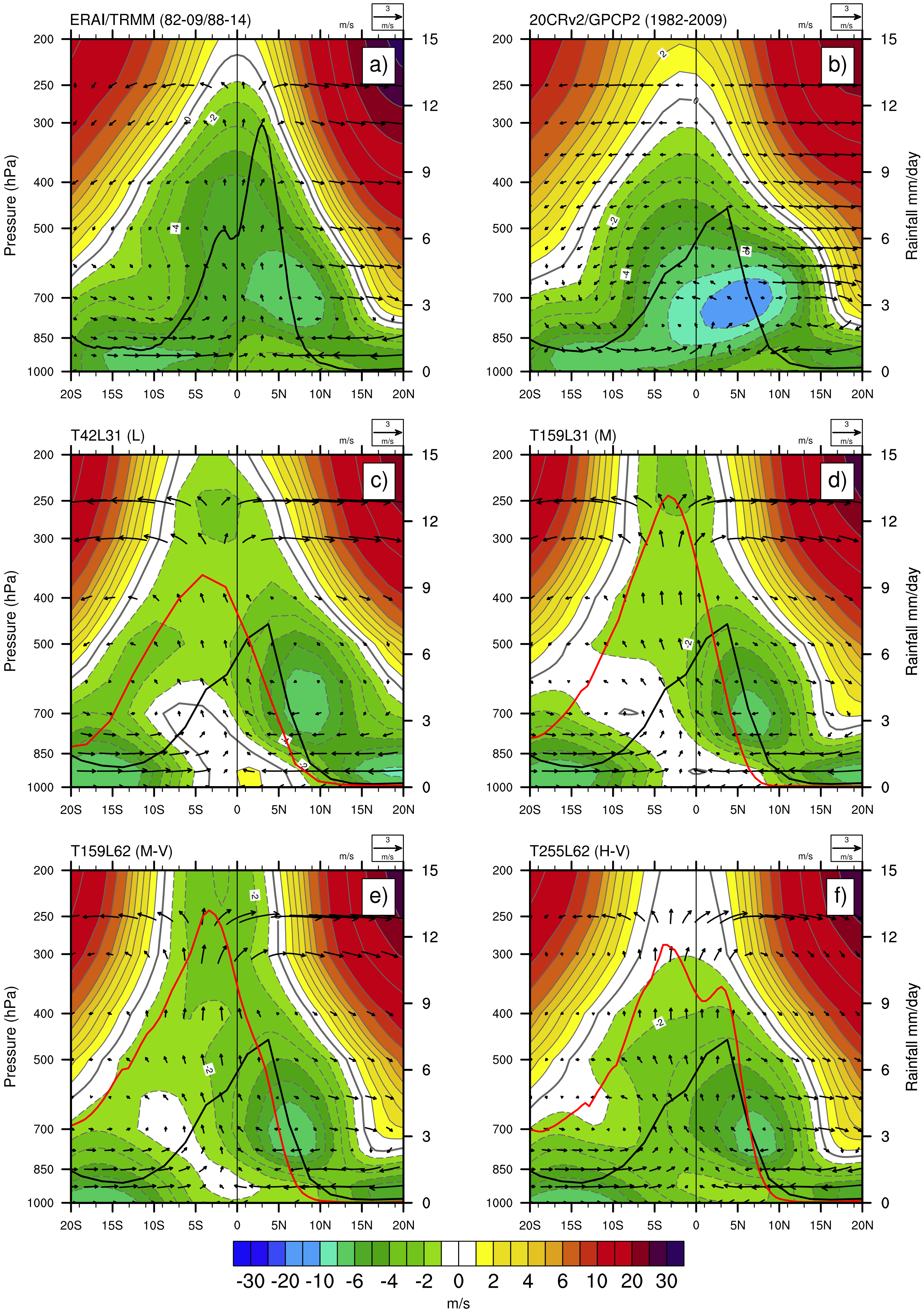

ERAI/TRMM (82-09/88-14)
a)
20CRv2/GPCP2 (1982-2009)
b)
T42L31 (L)
c)
T159L31 (M)
d)
T159L62 (M-V)
e)
T255L62 (H-V)
f)
3
m/s
Pressure (hPa)
Rainfall mm/day
200
250
300
400
500
700
850
1000
0
3
6
9
12
15
20S
15S
10S
5S
0
5N
10N
15N
20N
-30
-20
-10
-6
-4
-2
0
2
4
6
10
20
30
m/s

Figure 5

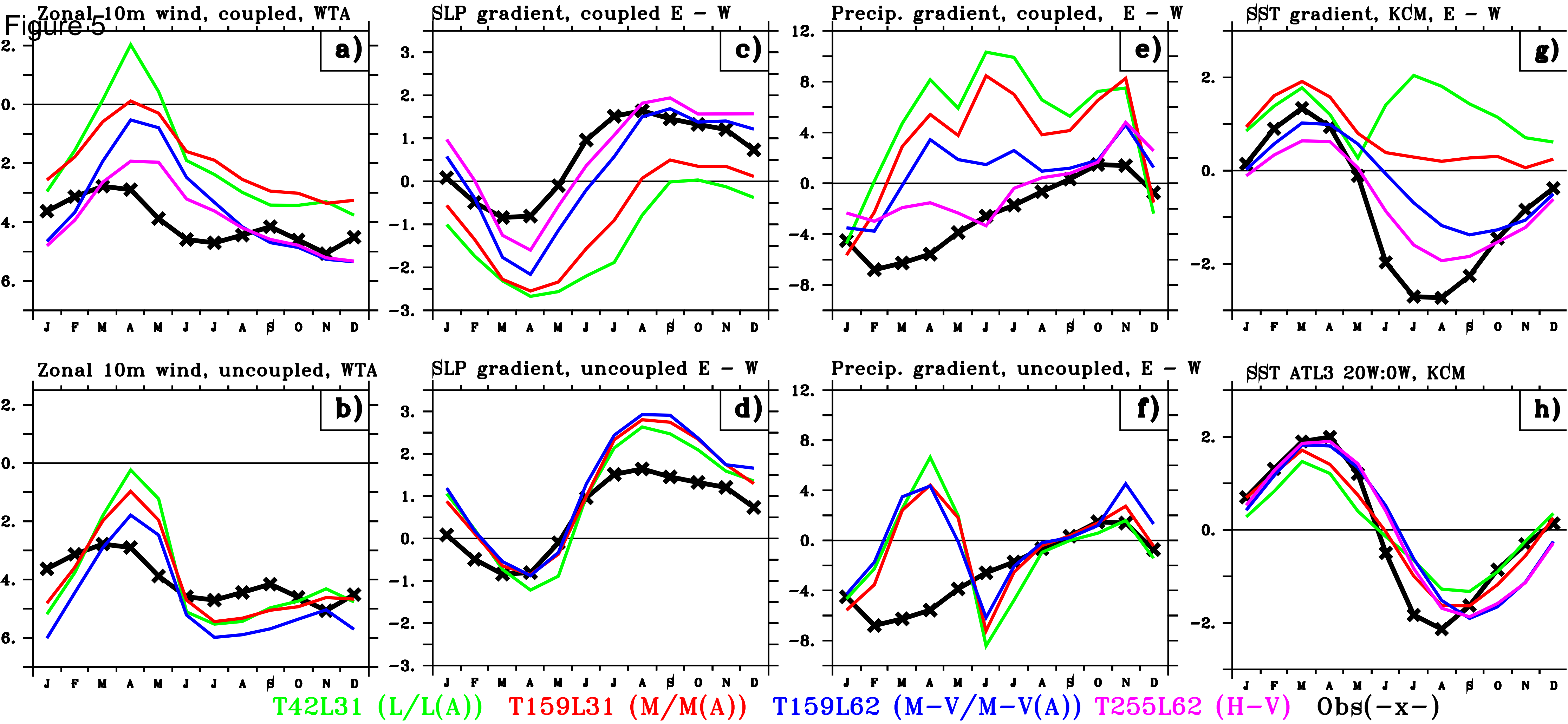
Zonal 10m wind, coupled, WTA
a)
SLP gradient, coupled E – W
c)
Precip. gradient, coupled, E – W
e)
SST gradient, KCM, E – W
g)
Zonal 10m wind, uncoupled, WTA
b)
SLP gradient, uncoupled E – W
d)
Precip. gradient, uncoupled, E – W
f)
SST ATL3 20W:0W, KCM
h)
2.
0.
-2.
-4.
-6.
3.
1.
-1.
-3.
12.
8.
4.
-4.
-8.
J F M A M J J A S O N D
T42L31 (L/L(A))
T159L31 (M/M(A))
T159L62 (M-V/M-V(A))
T255L62 (H-V)
Obs(-x-)

Figure 6

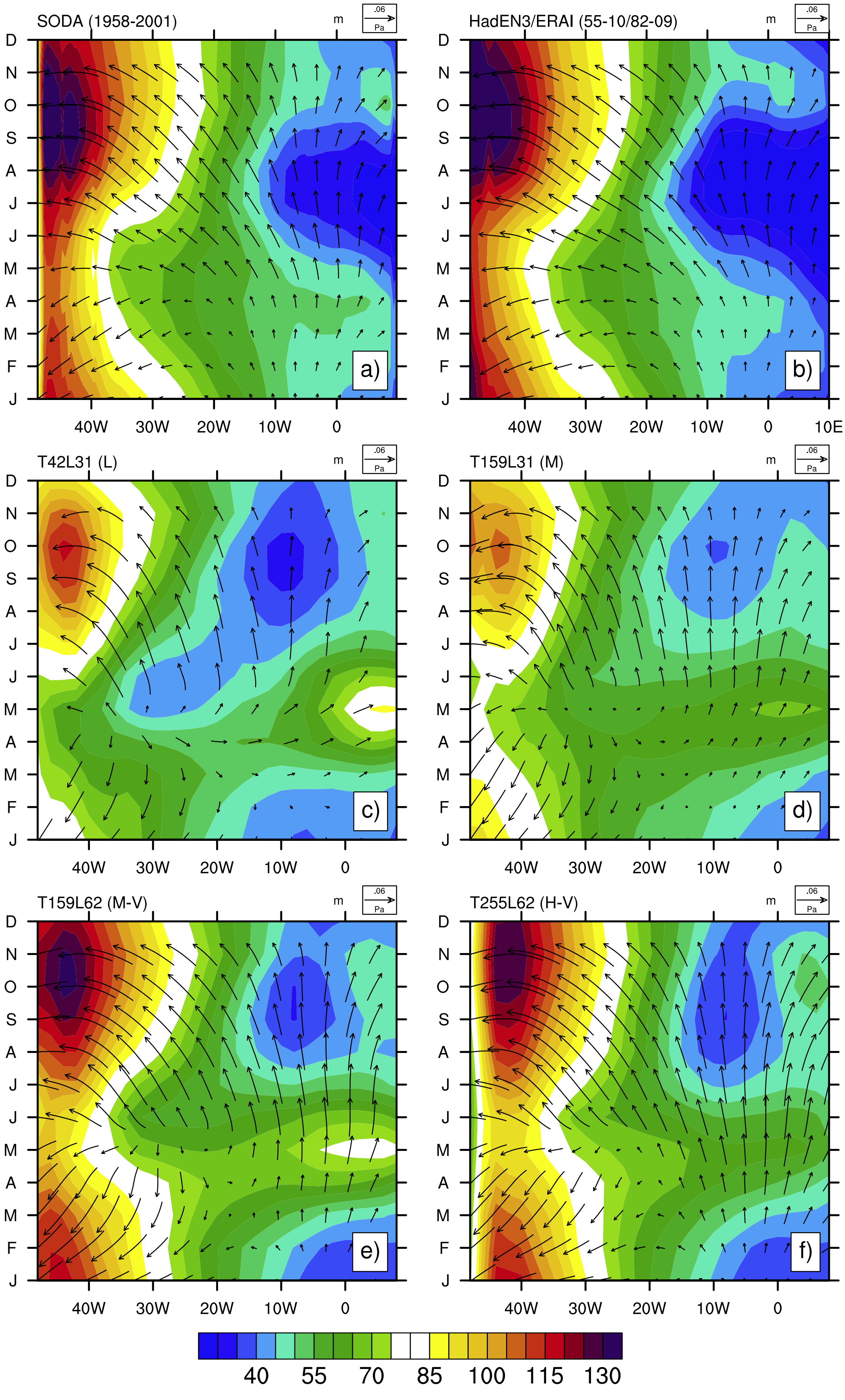
SODA (1958-2001)
HadEN3/ERAI (55-10/82-09)
T42L31 (L)
T159L31 (M)
T159L62 (M-V)
T255L62 (H-V)
m
.06
Pa
D
N
O
S
A
J
J
M
A
M
F
J
40W
30W
20W
10W
0
10E
a)
b)
c)
d)
e)
f)
40
55
70
85
100
115
130

Figure 7

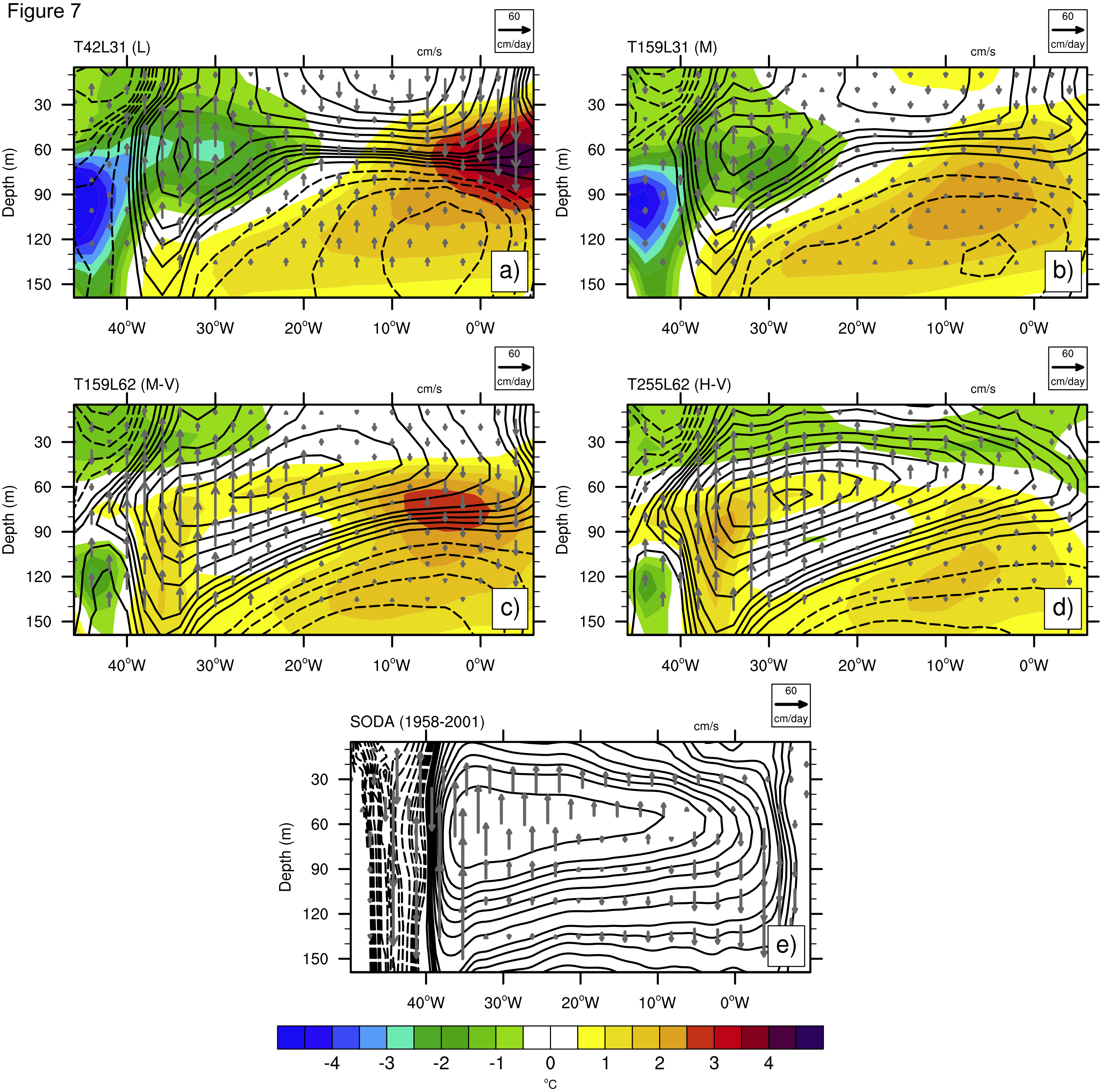
T42L31 (L)
T159L31 (M)
T159L62 (M-V)
T255L62 (H-V)
SODA (1958-2001)
60
cm/day
cm/s
Depth (m)
30
60
90
120
150
40°W
30°W
20°W
10°W
0°W
a)
b)
c)
d)
e)
-4
-3
-2
-1
0
1
2
3
4
°C

Figure 8

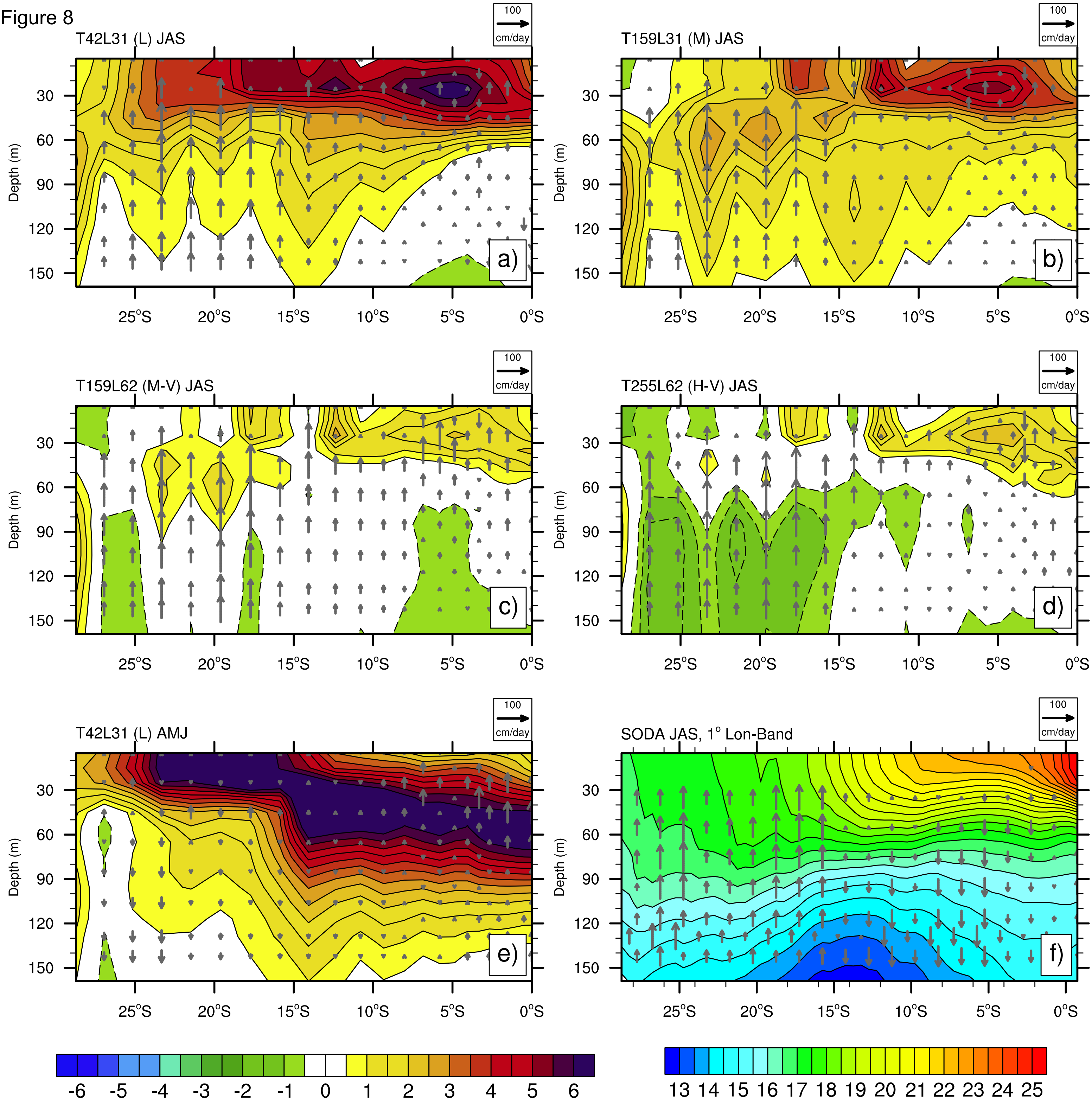

T42L31 (L) JAS
T159L31 (M) JAS
T159L62 (M-V) JAS
T255L62 (H-V) JAS
T42L31 (L) AMJ
SODA JAS, 1° Lon-Band
100
cm/day
Depth (m)
30
60
90
120
150
25°S
20°S
15°S
10°S
5°S
0°S
a)
b)
c)
d)
e)
f)
-6 -5 -4 -3 -2 -1 0 1 2 3 4 5 6
13 14 15 16 17 18 19 20 21 22 23 24 25

Figure 9

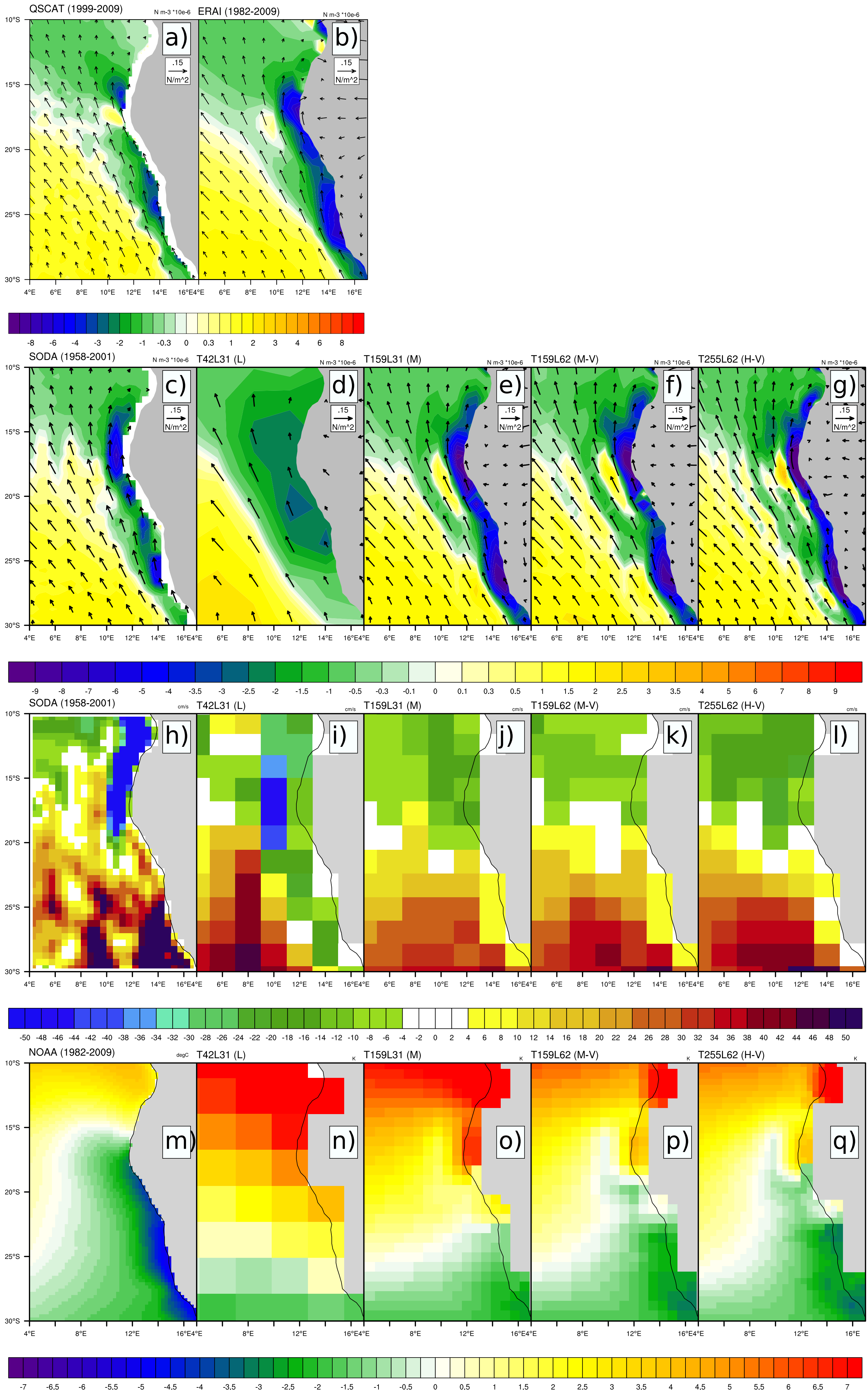
QSCAT (1999-2009)
N m-3 *10e-6
a)
ERAI (1982-2009)
N m-3 *10e-6
b)
.15
N/m^2
10°S
15°S
20°S
25°S
30°S
4°E
6°E
8°E
10°E
12°E
14°E
16°E
-8
-6
-4
-3
-2
-1
-0.3
0
0.3
1
2
3
4
6
8
SODA (1958-2001)
N m-3 *10e-6
c)
T42L31 (L)
d)
T159L31 (M)
e)
T159L62 (M-V)
f)
T255L62 (H-V)
g)
-9
-8
-7
-6
-5
-4
-3.5
-3
-2.5
-2
-1.5
-1
-0.5
-0.3
-0.1
0
0.1
0.3
0.5
1
1.5
2
2.5
3
3.5
4
5
6
7
8
9
SODA (1958-2001)
cm/s
h)
T42L31 (L)
i)
T159L31 (M)
j)
T159L62 (M-V)
k)
T255L62 (H-V)
l)
-50
-48
-46
-44
-42
-40
-38
-36
-34
-32
-30
-28
-26
-24
-22
-20
-18
-16
-14
-12
-10
-8
-6
-4
-2
0
2
4
6
8
10
12
14
16
18
20
22
24
26
28
30
32
34
36
38
40
42
44
46
48
50
NOAA (1982-2009)
degC
m)
T42L31 (L)
K
n)
T159L31 (M)
o)
T159L62 (M-V)
p)
T255L62 (H-V)
q)
-7
-6.5
-6
-5.5
-5
-4.5
-4
-3.5
-3
-2.5
-2
-1.5
-1
-0.5
0
0.5
1
1.5
2
2.5
3
3.5
4
4.5
5
5.5
6
6.5
7

Figure 10

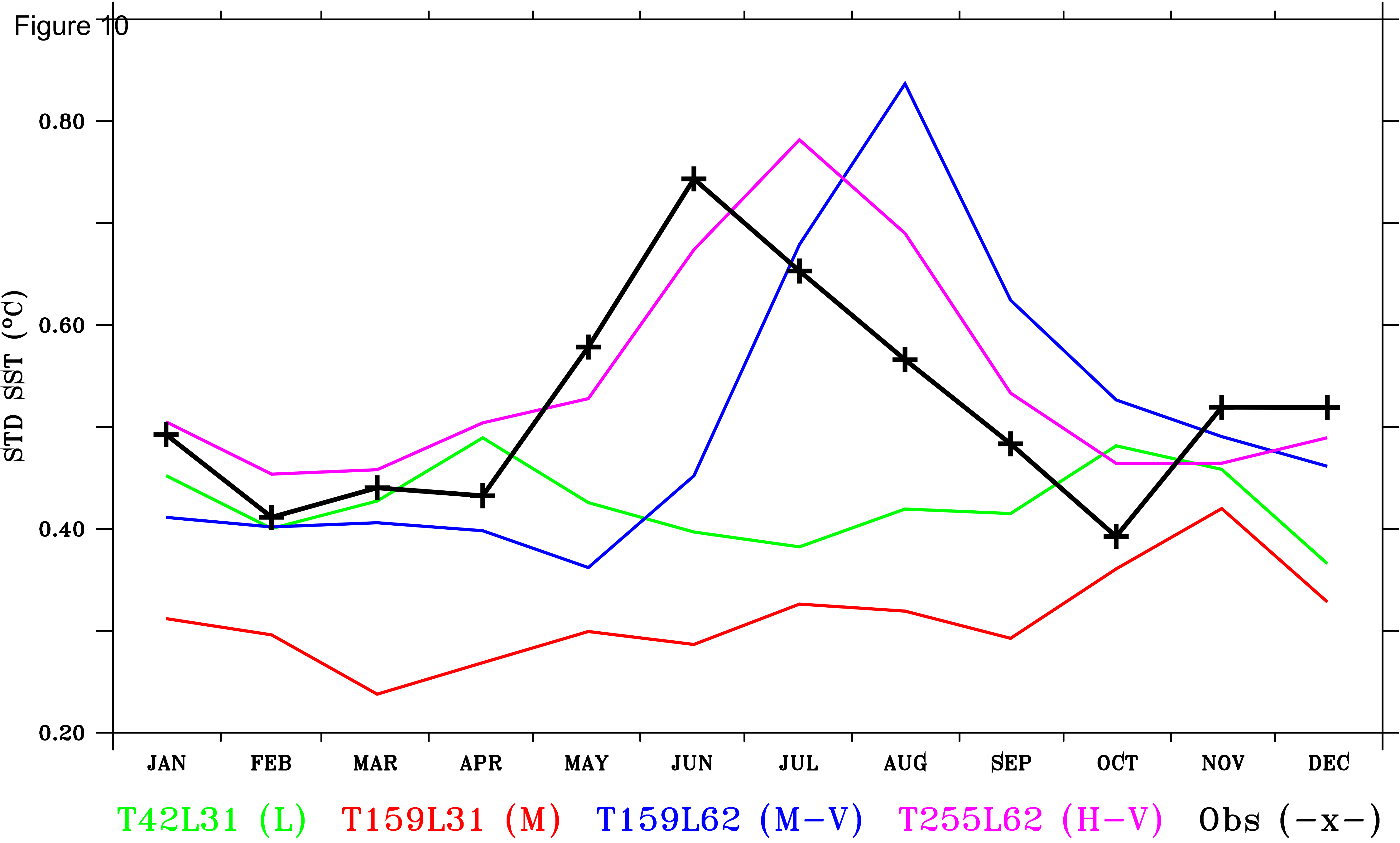
STD SST (°C)
0.80
0.60
0.40
0.20
JAN
FEB
MAR
APR
MAY
JUN
JUL
AUG
SEP
OCT
NOV
DEC
T42L31 (L)
T159L31 (M)
T159L62 (M-V)
T255L62 (H-V)
Obs (-x-)

Figure 11

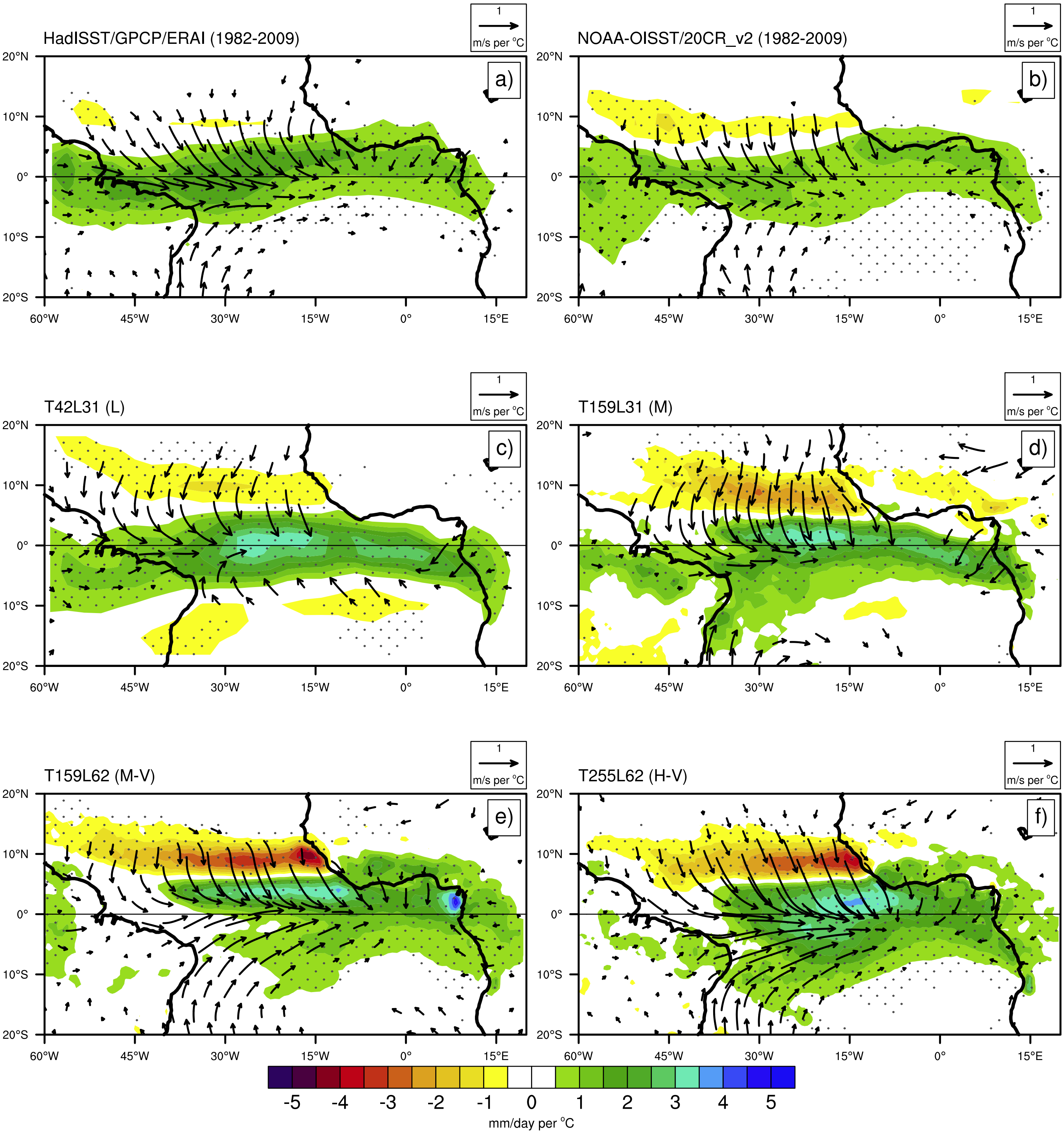
HadISST/GPCP/ERAI (1982-2009)
NOAA-OISST/20CR_v2 (1982-2009)
T42L31 (L)
T159L31 (M)
T159L62 (M-V)
T255L62 (H-V)
a)
b)
c)
d)
e)
f)
1
m/s per °C
20°N
10°N
0°
10°S
20°S
60°W
45°W
30°W
15°W
0°
15°E
-5
-4
-3
-2
-1
0
1
2
3
4
5
mm/day per °C

Figure 12

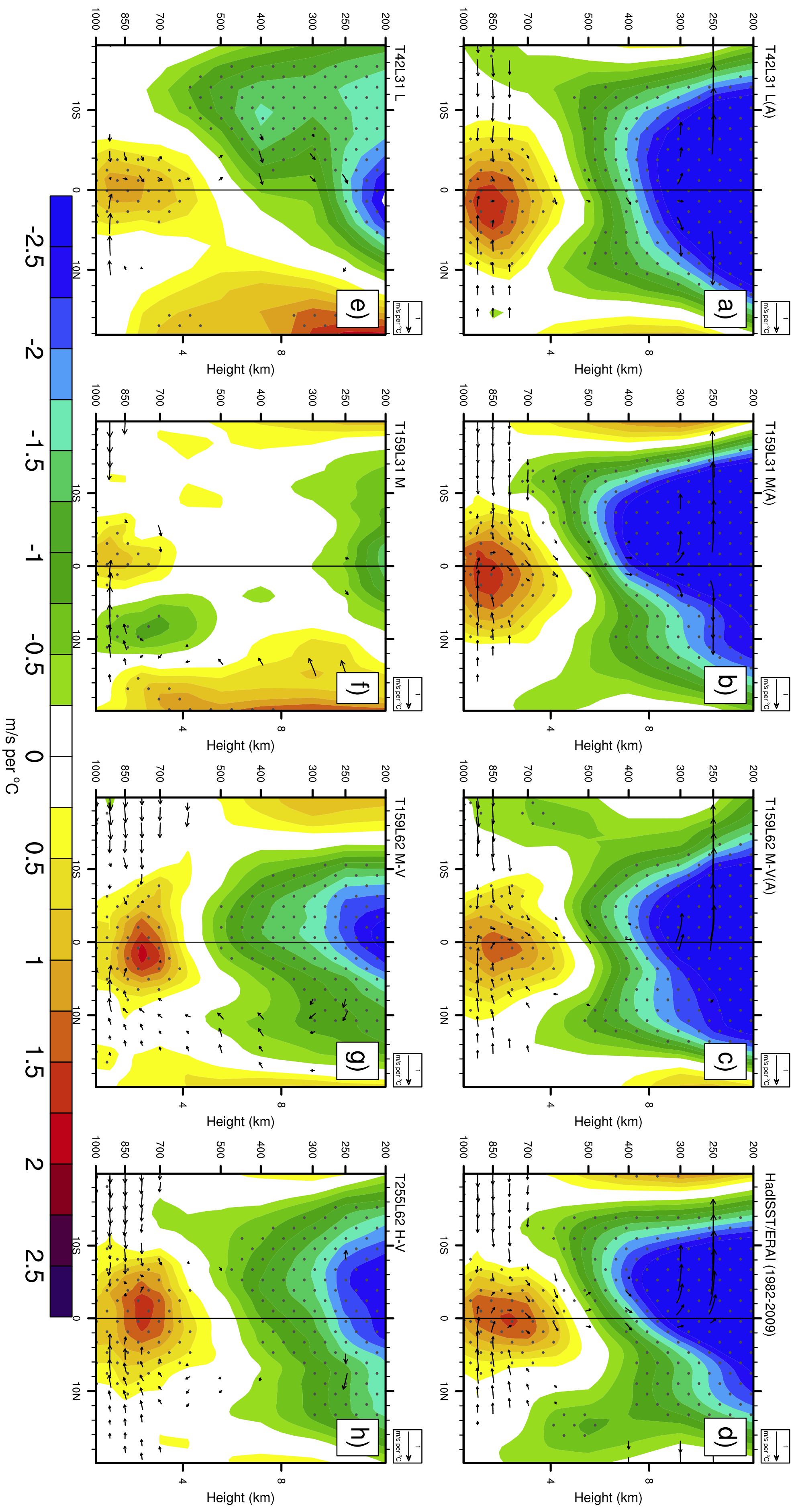
T42L31 L(A)
a)
T159L31 M(A)
b)
T159L62 M-V(A)
c)
HadISST/ERAI (1982-2009)
d)
T42L31 L
e)
T159L31 M
f)
T159L62 M-V
g)
T255L62 H-V
h)
1000
850
700
500
400
300
250
200
10S
0
10N
4
8
Height (km)
m/s per °C
-2.5
-2
-1.5
-1
-0.5
0
0.5
1
1.5
2
2.5

Figure 13

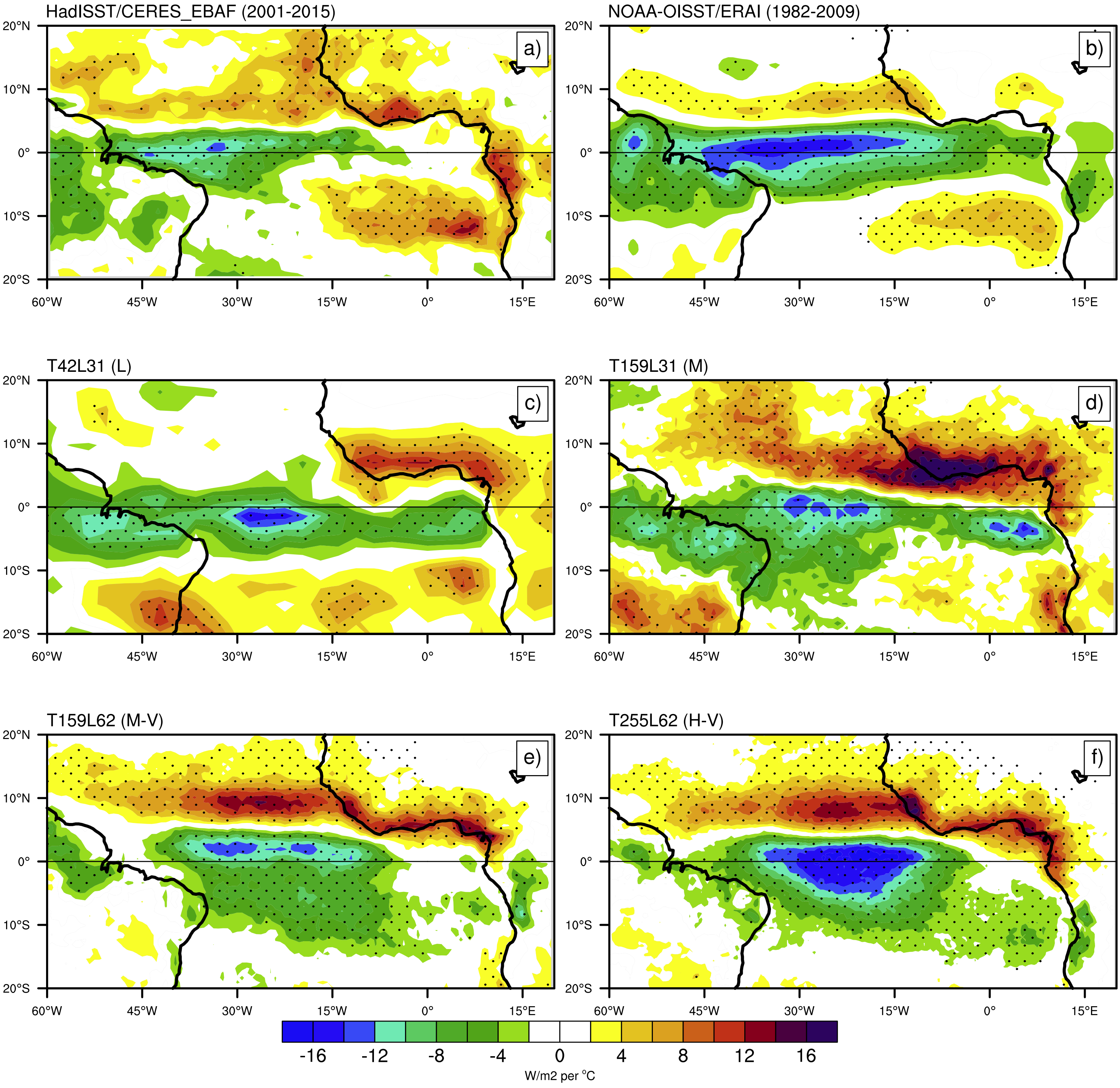

HadISST/CERES_EBAF (2001-2015)
a)
NOAA-OISST/ERAI (1982-2009)
b)
T42L31 (L)
c)
T159L31 (M)
d)
T159L62 (M-V)
e)
T255L62 (H-V)
f)
20°N
10°N
0°
10°S
20°S
60°W
45°W
30°W
15°W
0°
15°E
-16
-12
-8
-4
0
4
8
12
16
W/m2 per °C

Figure 14

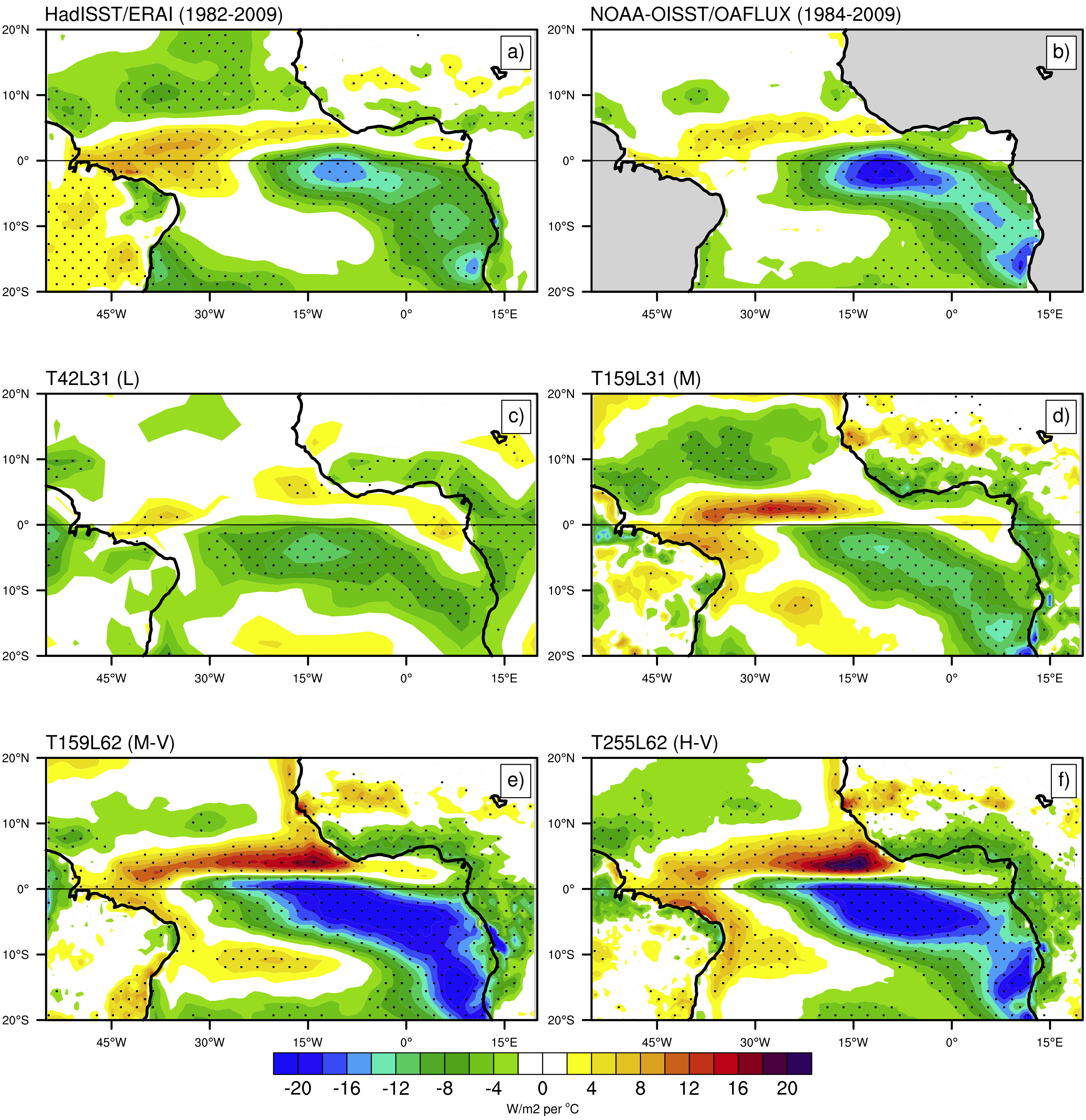
HadISST/ERAI (1982-2009)
a)
NOAA-OISST/OAFLUX (1984-2009)
b)
T42L31 (L)
c)
T159L31 (M)
d)
T159L62 (M-V)
e)
T255L62 (H-V)
f)
20°N
10°N
0°
10°S
20°S
45°W
30°W
15°W
0°
15°E
-20
-16
-12
-8
-4
0
4
8
12
16
20
W/m2 per °C

Figure 15

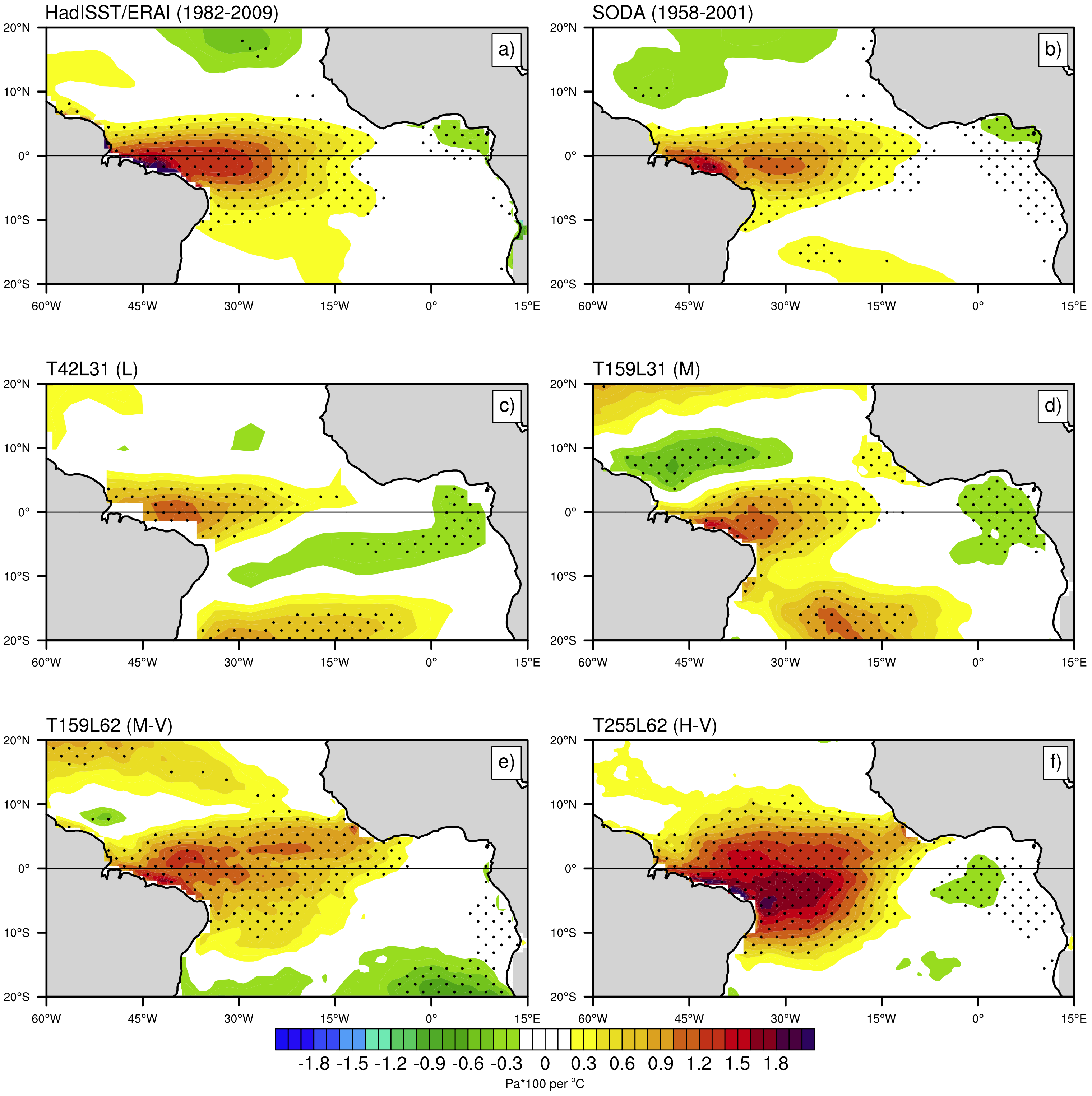

HadISST/ERAI (1982-2009)
a)
SODA (1958-2001)
b)
T42L31 (L)
c)
T159L31 (M)
d)
T159L62 (M-V)
e)
T255L62 (H-V)
f)
20°N
10°N
0°
10°S
20°S
60°W
45°W
30°W
15°W
0°
15°E
-1.8 -1.5 -1.2 -0.9 -0.6 -0.3 0 0.3 0.6 0.9 1.2 1.5 1.8
Pa*100 per °C

Figure 16

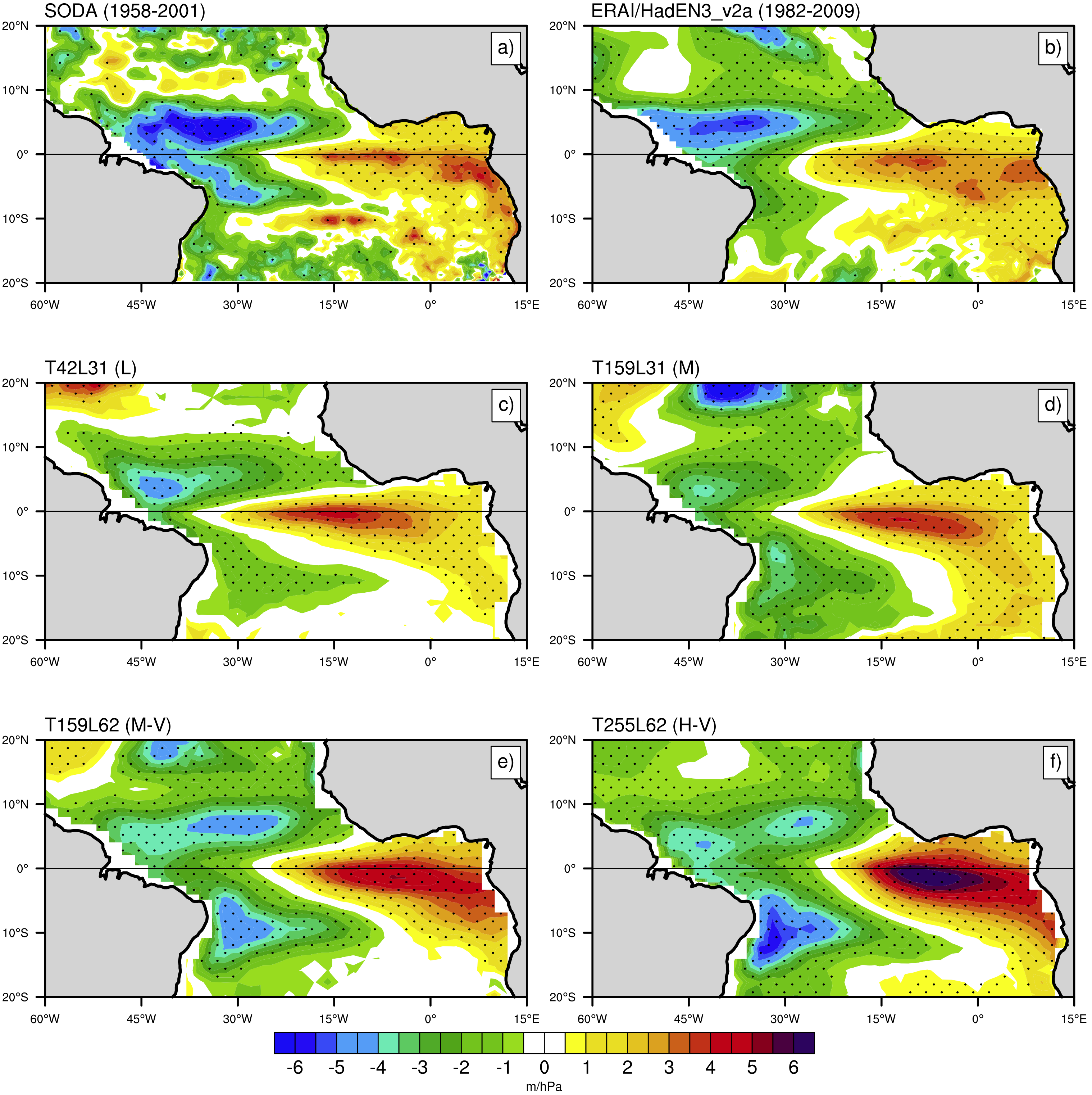
SODA (1958-2001)
a)
ERAI/HadEN3_v2a (1982-2009)
b)
T42L31 (L)
c)
T159L31 (M)
d)
T159L62 (M-V)
e)
T255L62 (H-V)
f)
20°N
10°N
0°
10°S
20°S
60°W
45°W
30°W
15°W
0°
15°E
-6
-5
-4
-3
-2
-1
0
1
2
3
4
5
6
m/hPa

Figure 17

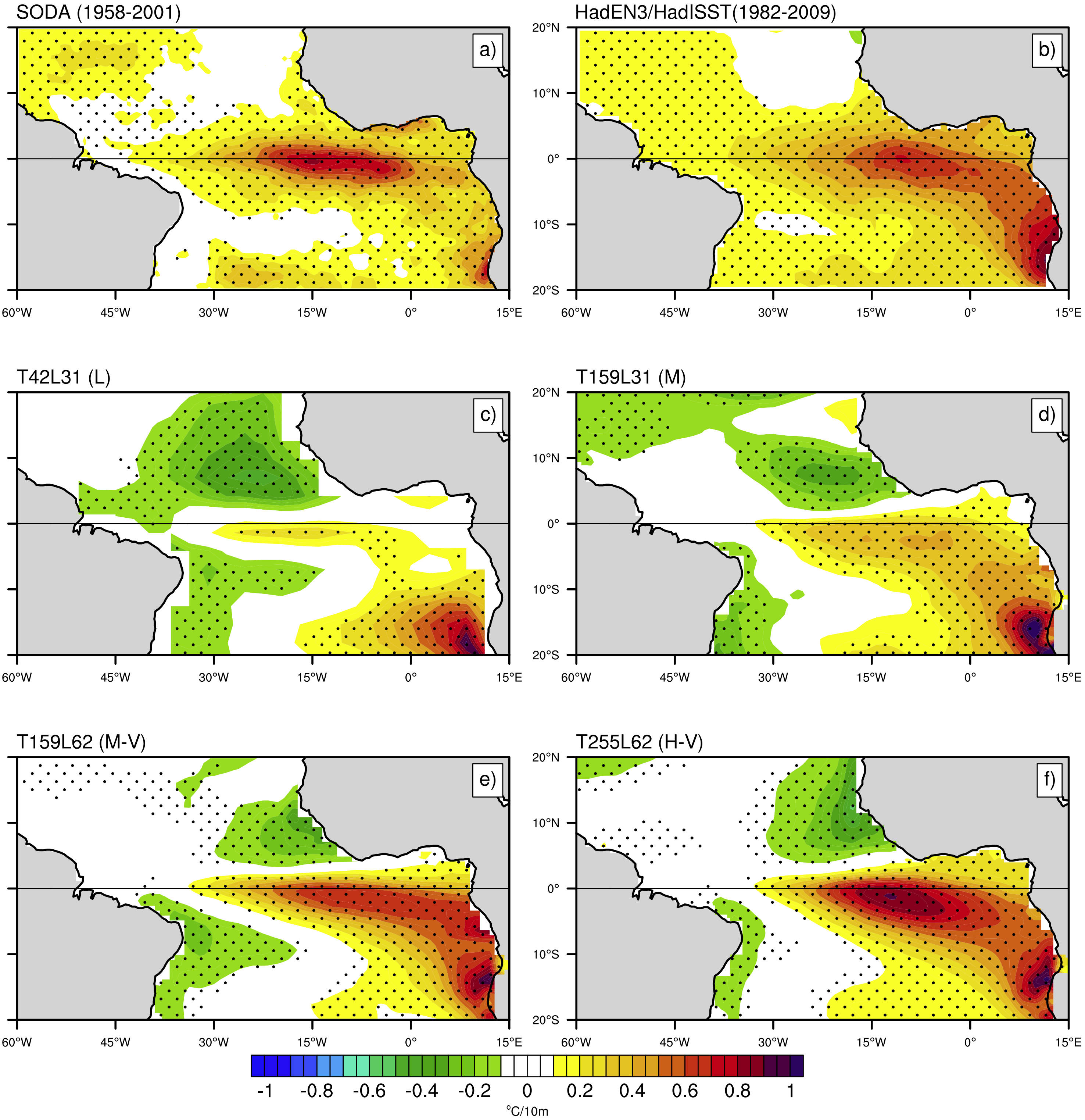

SODA (1958-2001)
HadEN3/HadISST(1982-2009)
T42L31 (L)
T159L31 (M)
T159L62 (M-V)
T255L62 (H-V)
a)
b)
c)
d)
e)
f)
20°N
10°N
0°
10°S
20°S
60°W
45°W
30°W
15°W
0°
15°E
-1
-0.8
-0.6
-0.4
-0.2
0
0.2
0.4
0.6
0.8
1
°C/10m

Figure 18

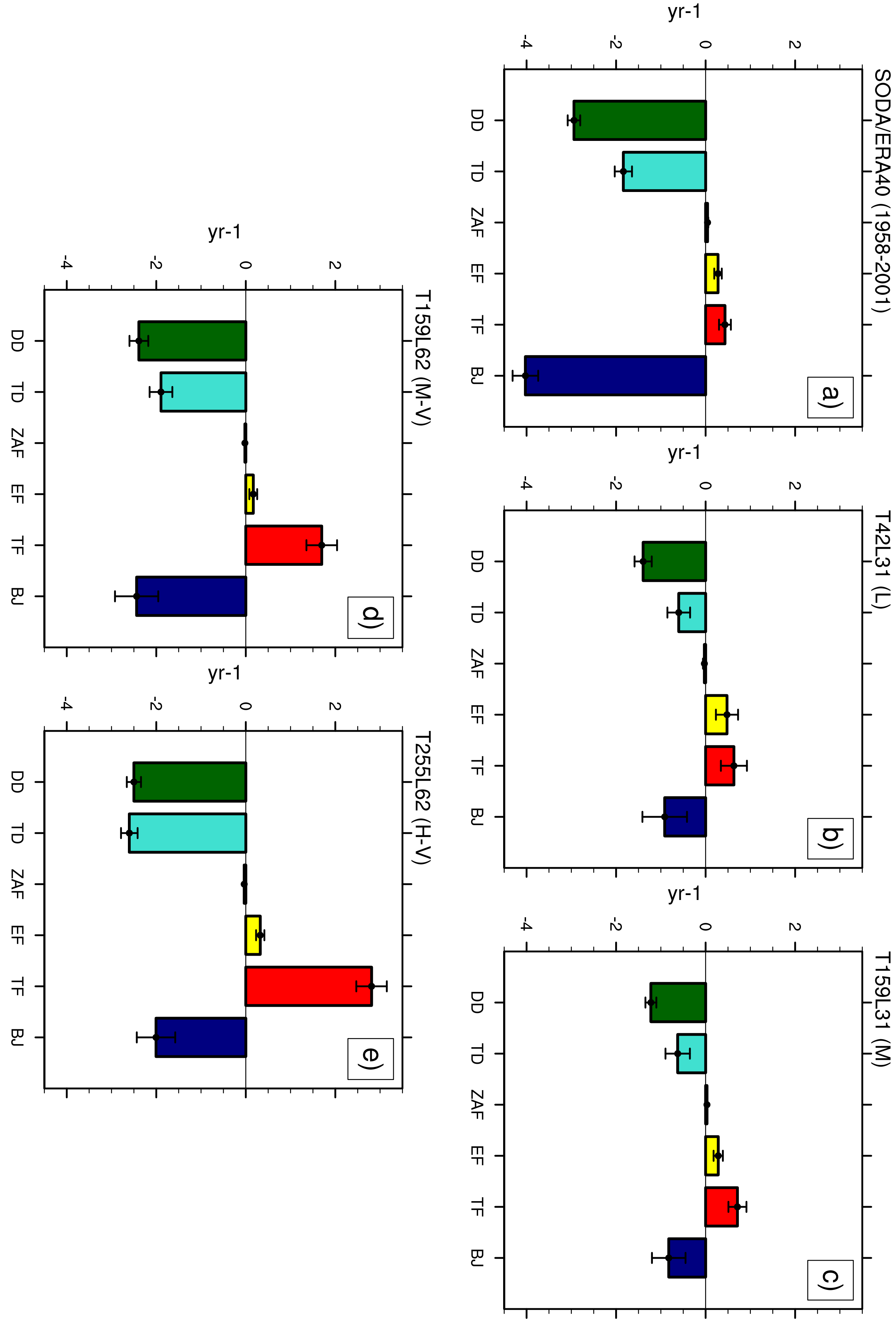
SODA/ERA40 (1958-2001)
T42L31 (L)
T159L31 (M)
T159L62 (M-V)
T255L62 (H-V)
a)
b)
c)
d)
e)
yr-1
2
0
-2
-4
DD
TD
ZAF
EF
TF
BJ

Figure S1

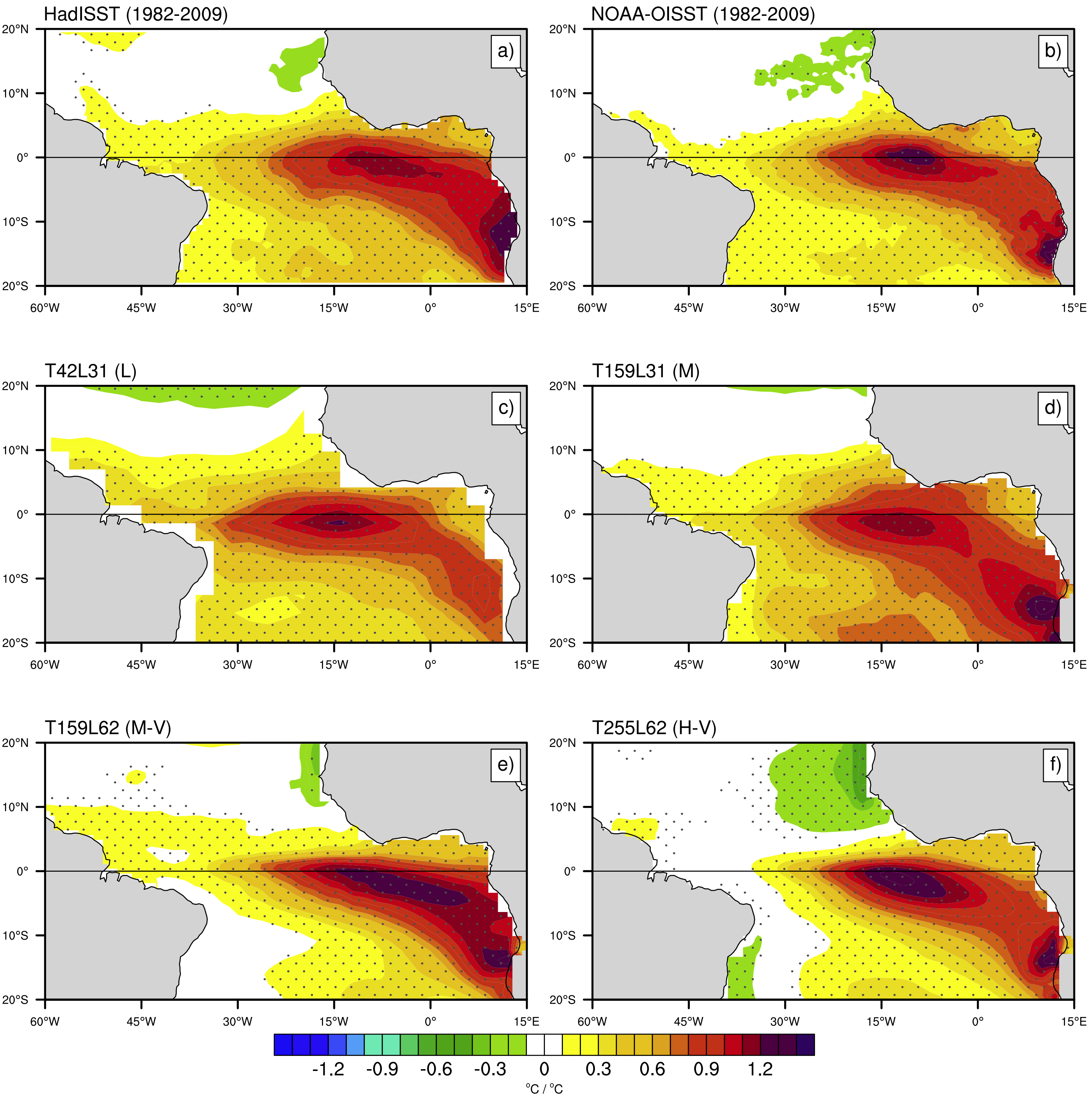
HadISST (1982-2009)
NOAA-OISST (1982-2009)
T42L31 (L)
T159L31 (M)
T159L62 (M-V)
T255L62 (H-V)
a)
b)
c)
d)
e)
f)
20°N
10°N
0°
10°S
20°S
60°W
45°W
30°W
15°W
0°
15°E
-1.2
-0.9
-0.6
-0.3
0
0.3
0.6
0.9
1.2
°C / °C

Figure S2

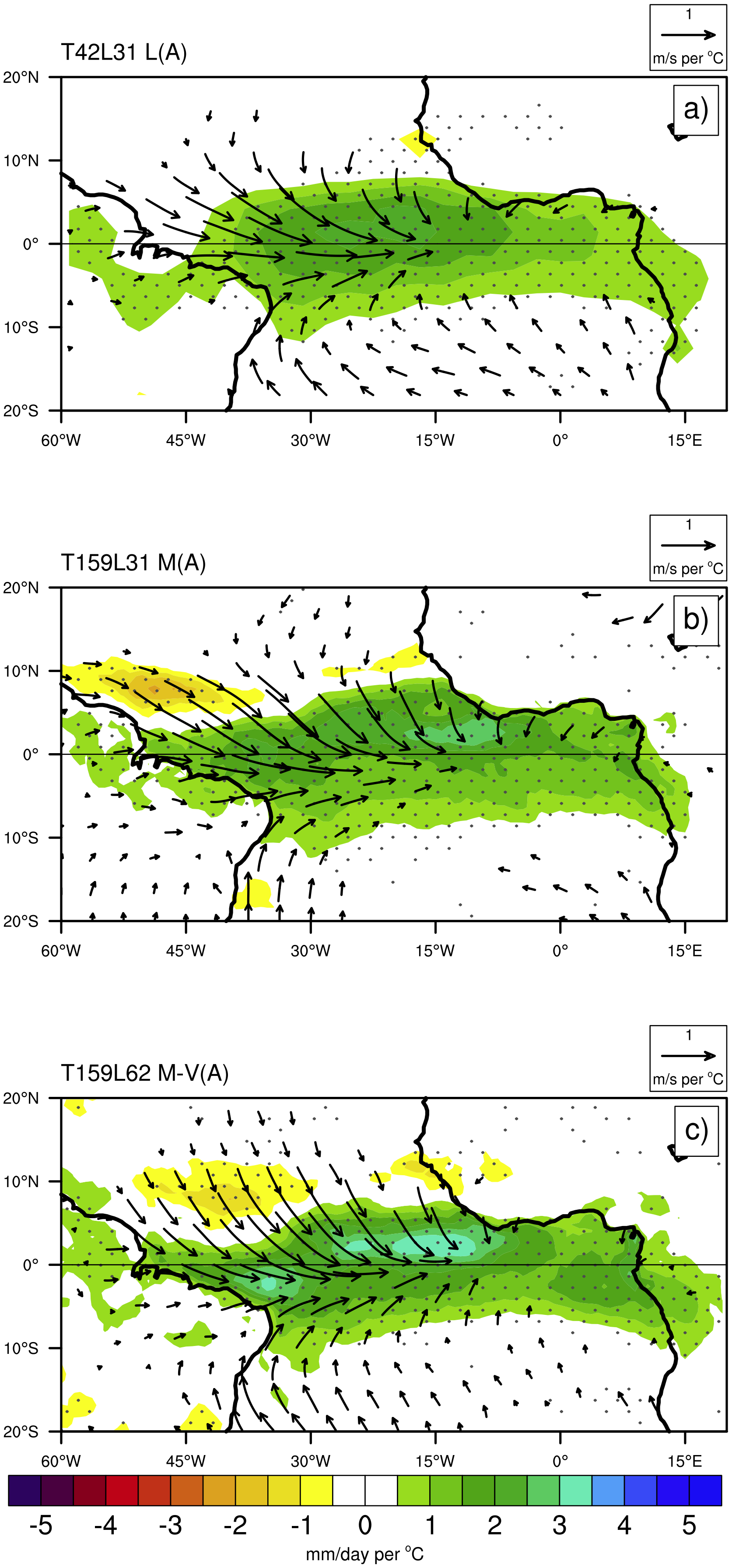
T42L31 L(A)
1
m/s per °C
a)
T159L31 M(A)
1
m/s per °C
b)
T159L62 M-V(A)
1
m/s per °C
c)
20°N
10°N
0°
10°S
20°S
60°W
45°W
30°W
15°W
0°
15°E
-5
-4
-3
-2
-1
0
1
2
3
4
5
mm/day per °C

Figure S3

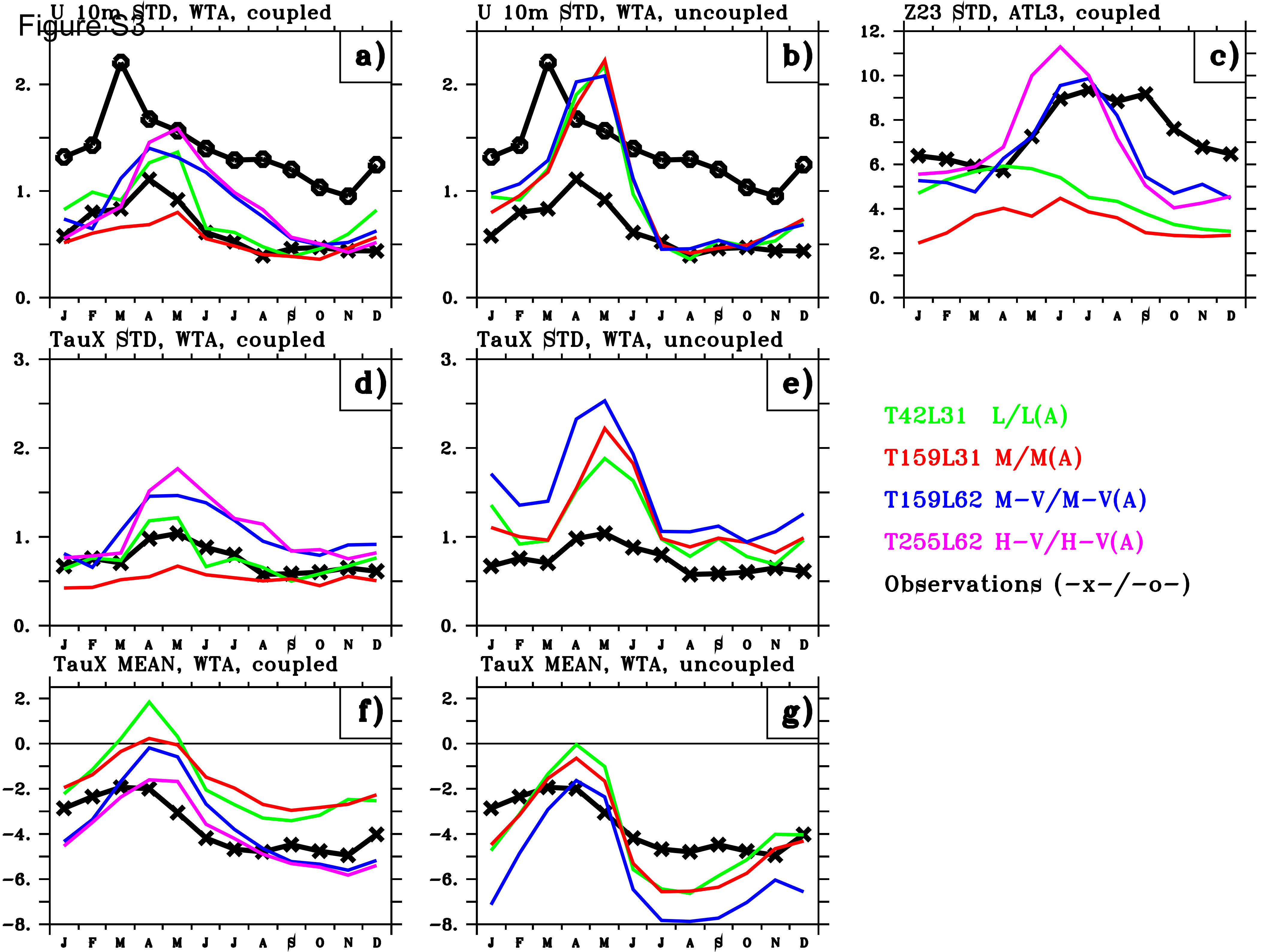
U 10m STD, WTA, coupled
a)
U 10m STD, WTA, uncoupled
b)
Z23 STD, ATL3, coupled
c)
TauX STD, WTA, coupled
d)
TauX STD, WTA, uncoupled
e)
TauX MEAN, WTA, coupled
f)
TauX MEAN, WTA, uncoupled
g)
0.
1.
2.
3.
0.
2.
4.
6.
8.
10.
12.
−8.
−6.
−4.
−2.
0.0
2.
J F M A M J J A S O N D
T42L31 L/L(A)
T159L31 M/M(A)
T159L62 M−V/M−V(A)
T255L62 H−V/H−V(A)
Observations (−x−/−o−)

Figure S4

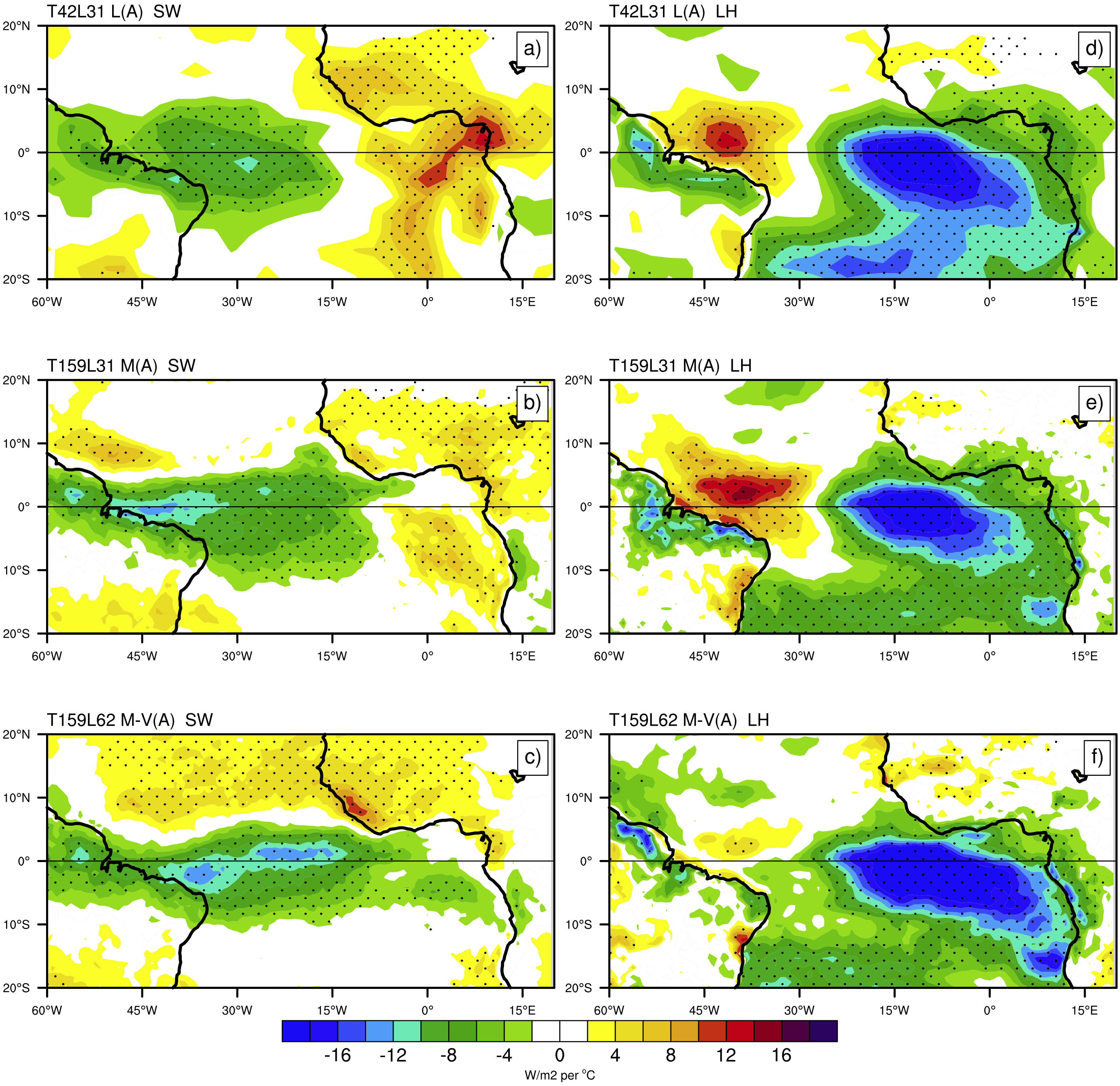

T42L31 L(A) SW

T42L31 L(A) LH

T159L31 M(A) SW

T159L31 M(A) LH

T159L62 M-V(A) SW

T159L62 M-V(A) LH

Figure S5

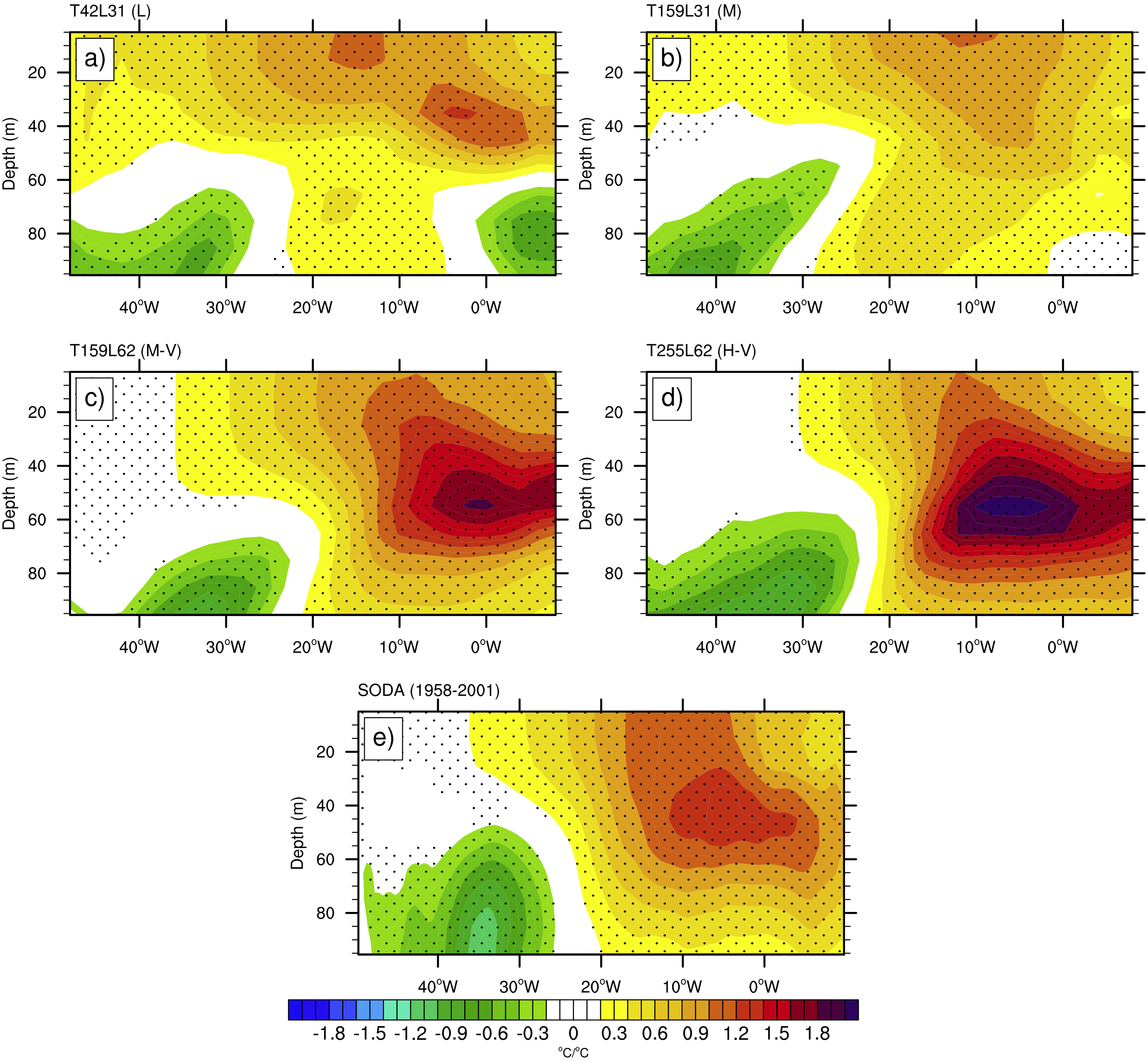
T42L31 (L)
a)
T159L31 (M)
b)
T159L62 (M-V)
c)
T255L62 (H-V)
d)
SODA (1958-2001)
e)
Depth (m)
20
40
60
80
40°W
30°W
20°W
10°W
0°W
-1.8
-1.5
-1.2
-0.9
-0.6
-0.3
0
0.3
0.6
0.9
1.2
1.5
1.8
°C/°C

Figure S6

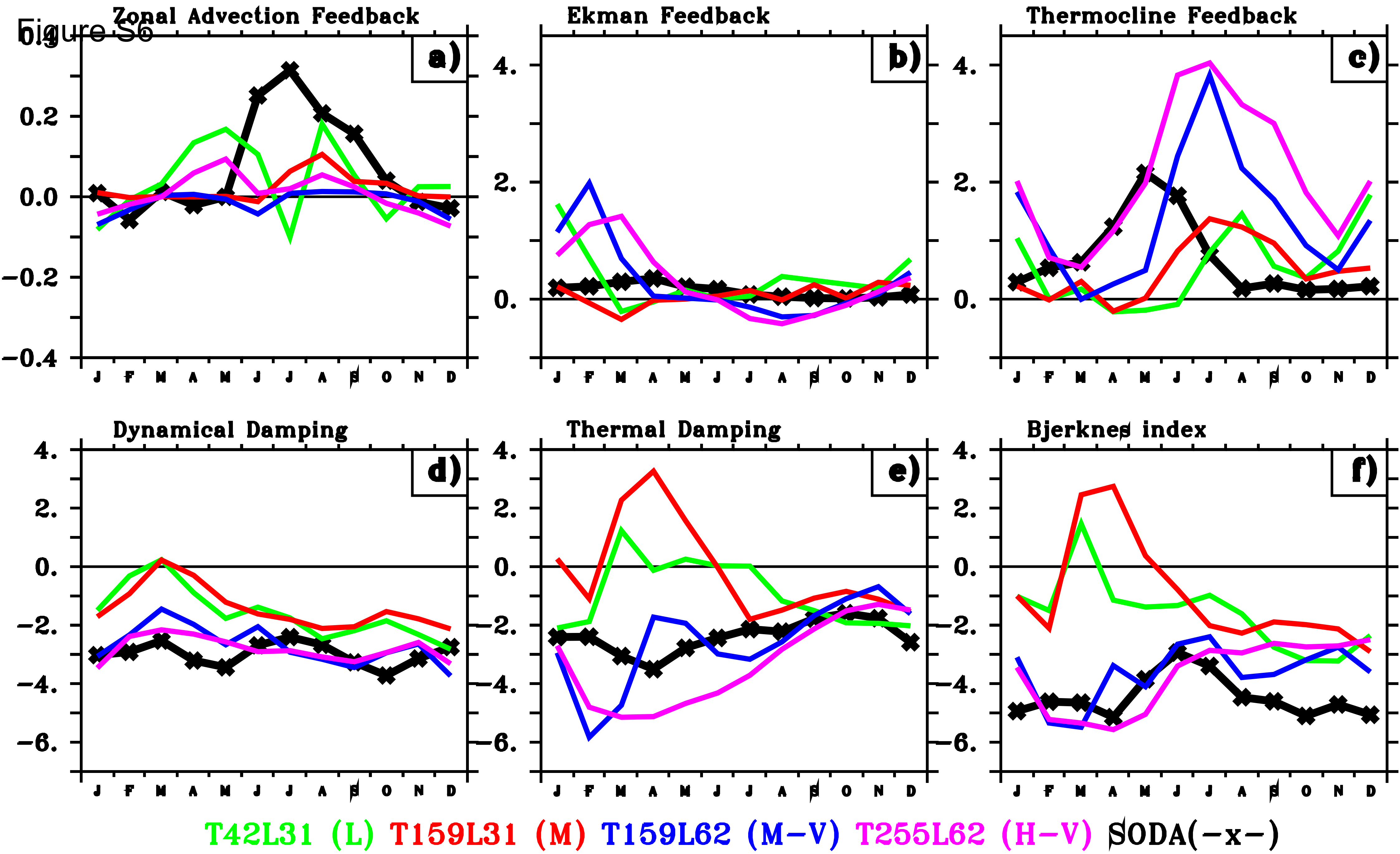
Zonal Advection Feedback
a)
0.4
0.2
0.0
−0.2
−0.4
J F M A M J J A S O N D
Ekman Feedback
b)
4.
2.
0.
J F M A M J J A S O N D
Thermocline Feedback
c)
4.
2.
0.
J F M A M J J A S O N D
Dynamical Damping
d)
4.
2.
0.
−2.
−4.
−6.
J F M A M J J A S O N D
Thermal Damping
e)
4.
2.
0.
−2.
−4.
−6.
J F M A M J J A S O N D
Bjerknes index
f)
4.
2.
0.
−2.
−4.
−6.
J F M A M J J A S O N D
T42L31 (L) T159L31 (M) T159L62 (M−V) T255L62 (H−V) SODA(−x−)